GEOLOGICA CARPATHICA, OCTOBER 2019, 70, 5, 386–404 doi: 10.2478/geoca-2019-0022

New $^{40}Ar/^{39}Ar$, fission track and sedimentological data on a middle Miocene tuff occurring in the Vienna Basin: Implications for the north-western Central Paratethys region

SAMUEL RYBÁR[1,✉], KATARÍNA ŠARINOVÁ[2], KARIN SANT[3], KLAUDIA F. KUIPER[4], MARIANNA KOVÁČOVÁ[1], RASTISLAV VOJTKO[1], MARTIN K. REISER[5,7], KLEMENT FORDINÁL[6], VASILIS TEODORIDIS[8], PETRONELA NOVÁKOVÁ[1] and TOMÁŠ VLČEK[1]

[1]Department of Geology and Paleontology, Comenius University in Bratislava, Mlynská dolina, Ilkovičova 6, 842 15 Bratislava, Slovakia; ✉samuelrybar3@gmail.com
[2]Department of Mineralogy and Petrology, Comenius University in Bratislava, Mlynská dolina, Ilkovičova 6, 842 15 Bratislava, Slovakia
[3]Paleomagnetic Laboratory Fort Hoofddijk, Utrecht University, Budapestlaan 4, Utrecht, Netherlands
[4]Vrije Universiteit Amsterdam, Department of Earth Sciences, Faculty of Science, De Boelelaan 1085, 1081HV Amsterdam, Netherlands
[5]Department of Geology, University of Innsbruck, Innrain 52f, 6020 Innsbruck, Austria
[6]State Geological Institute of Dionýz Štúr, Mlynská dolina 1, 817 04 Bratislava, Slovakia
[7]Geologische Bundesanstalt, Neulinggasse 38, 1030 Wien, Austria
[8]Department of Biology and Environmental Studies, Charles University, M. Rettigové 4, 116 39 Prague, Czech Republic

(Manuscript received July 30, 2018; accepted in revised form September 18, 2019)

Abstract: The Kuchyňa tuff is found on the Eastern margin of the Vienna Basin and was formed by felsic volcanism. The Ar/Ar single grain sanidine method was applied and resulted in an age of 15.23±0.04 Ma, which can be interpreted as the age of the eruption. The obtained numerical age is in accordance with the subtropical climate inferred by the presence of fossil leaves that originated in an evergreen broadleaved forest. Furthermore, the described volcanism was connected with the syn-rift stage of the back-arc Pannonian Basin system. The sedimentological data from the underlying sandy mudstones indicate alluvial environment what confirms terrestrial conditions during deposition. Moreover, the tuff deposition probably occurred shortly before the Badenian transgression of the Central Paratethys Sea.

Key words: $^{40}Ar/^{39}Ar$ dating, fission track, Vienna Basin, middle Miocene.

Introduction

The analyzed Kuchyňa tuff (Šimon et al. 2009) was found during geological mapping of Cenozoic sediments in the Vienna Basin (Lat: 48.396428°, Lon: 17.164325°; Fig. 1). The outcrop is localized in a wall of a deep scour and it is the only known tuff section in this region. The total thickness of the tuff was estimated as 30 cm (Fordinál et al. 2010). This tuff was originally described as fine-grained and composed of plagioclase, biotite, quartz, orthopyroxene, apatite, ilmenite and titanomagnetite together with vesiculated rhyolitic vitroclasts in clay matrix (Šimon et al. 2009). The tuff also contains fossil leaf imprints, determined as *Daphnogene polymorpha*, *Juglans* sp., *Dicotylophyllum* sp., ?*Salix varians*, ?*Ampelopsis* sp., ?*Quercus* sp. and Lauraceae indet. (Fordinál et al. 2010).

The recent excavations concentrated on this unique tuff, with the ambition to extract additional information about the extent of the middle Miocene volcanic activity in the Carpathian–Pannonian Region. The main aim of this paper is to provide radiometric age data using the $^{40}Ar/^{39}Ar$ and fission track (FT) methods supplemented by paleobotanical data. Such age data in combination with information about chemical composition should enable a better understanding of the tectono-sedimentary evolution of the Vienna Basin. In addition, the age of the Kuchyňa tuff will allow stratigraphic calibration of the determined paleoecological conditions. Moreover, the tuff will serve as a chronostratigraphical marker within the NW Pannonian Basin system.

Geological setting

The study area extends in the Kuchyňa highland at the boundary between the Vienna Basin and the Malé Karpaty Mountains (Western Carpathian mountain range). The geological structure of the Malé Karpaty Mts. is divided into several tectonic units of Paleozoic to Mezozoic age. In the study area only Mesozoic sedimentary units are present (Fig. 1; Polák et al. 2012; Fordinál et al. 2012a). The Vienna Basin started its evolution in the early Miocene as a piggy back basin and later (middle and late Miocene) evolved into a forearc basin (Kováč 2000; Vass 2002; Fordinál et al. 2012a). The Miocene infill of the Vienna Basin in the study area is assigned to the Devínska Nová Ves Fm. (Fordinál et al. 2012a; Fig. 1). This formation is represented by breccias and conglomerates, rusty coloured to spotty clays, coaly clays, lignite beds, non-calcareous sands

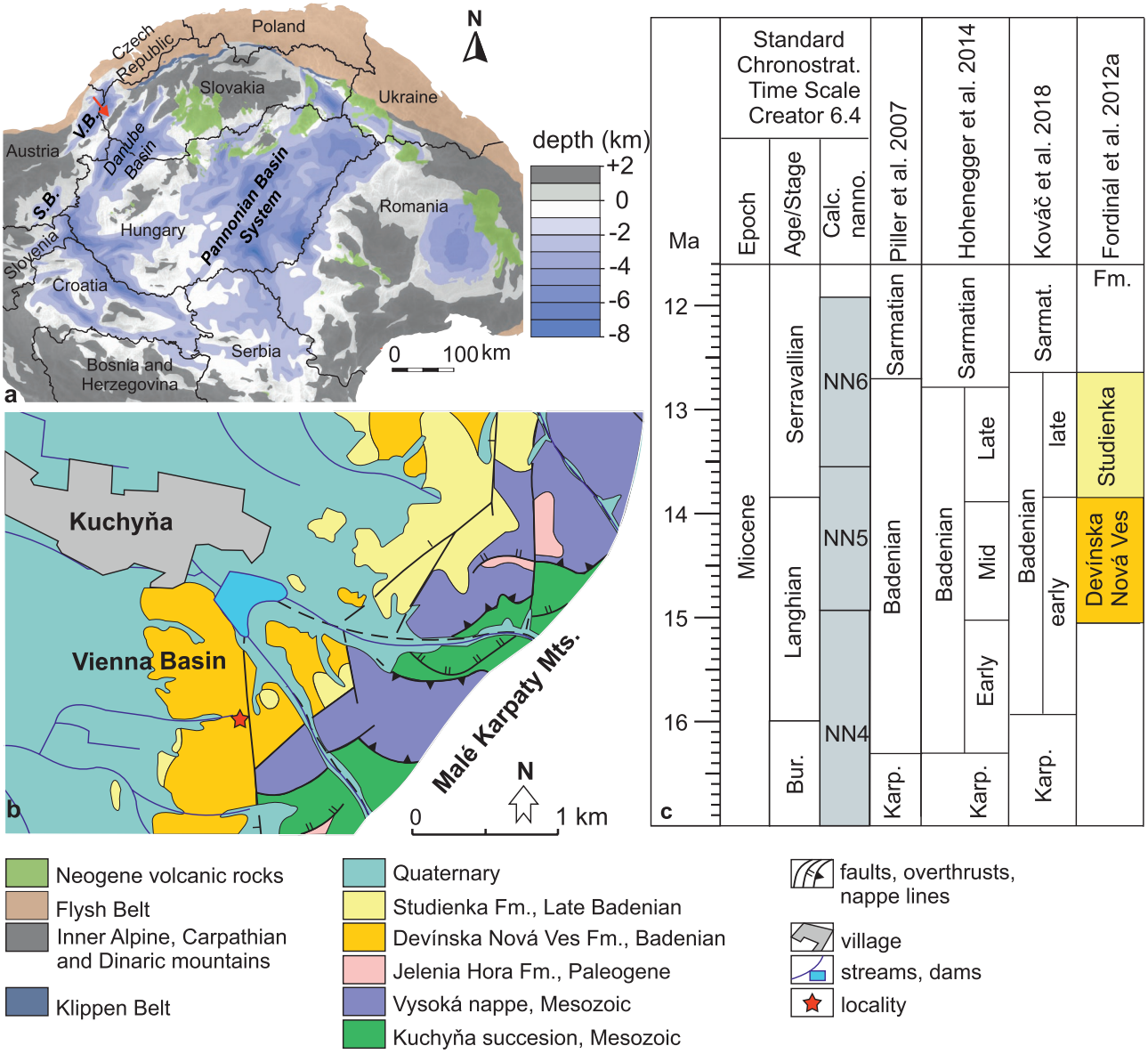

Fig. 1. Location map of the study area: **a** — location within the Pannonian Basin System; VB — Vienna Basin, SB — Styrian Basin, the red arrow indicates position of the study area; **b** — schematized geological map of the study area after Fordinál et al. (2012b); **c** — integrated Miocene chronostratigraphy.

and tuffs. The Devínska Nová Ves Fm. is either of middle Badenian age (late Langhian; Fordinál et al. 2010, 2012a), or of early Badenian age (Langhian) sense Kováč et al. (2007, 2018; Fig. 1). The paleoenvironment was described as terrestrial, alluvial to deltaic (Fordinál et al. 2010, 2012a; Polák et al. 2012). The formation is rarely overlain by conglomerates, gravels and mudstones of late Badenian age (Studienka Fm.; Fordinál et al. 2012a).

The middle Miocene volcanic fields in this region are connected to the rifting of back-arc basins in the north part of the Panonian Basin system (e.g. Kováč 2000; Konečný & Lexa 2002; Konečný et al. 2002b). The nearest volcanic centres are buried in the neighbouring Danube Basin (e.g., Hrušecký 1999; Kronome et al. 2014; Rybár et al. 2016). These centres were not dated radiometrically, except for the Rusovce volcanic centre, which was dated to 16.2±0.5 Ma (Kantor 1987) by using the whole rock K/Ar method. All of these centres are overlain by Badenian sediments (Miháliková 1962; Gaža 1966; Bondarenková 1980; Rybár et al. 2016), except for the Pásztori volcanic centre which is of middle to late Miocene age (Harangi et al. 1995). Moreover in the north-western part of the Danube Basin, several tuff horizons were dated biostratigraphically to the early Badenian (NN5; Rybár et al. 2016; Csibri et al. 2018). To the East, in the Central Slovak Volcanic field (Lexa et al. 2010), the volcanic activity starts with numerous volcanic centres located in shallow water conditions

(Neresnica, Vinica fms.). Their radiometric dating varies from 16.5–16 Ma (Konečný in Konečný et al. 1998) to 15 Ma (Chernyshev et al. 2013). The activity continued with evolution of volcanoes and stratovolcanoes (Konečný et al. 1998). The nearest exposed volcanic centre in the vicinity is the Štiavnica stratovolcano, which was active from ~15 to 11 Ma not counting the alkali basalt volcanism (Chernyshev et al. 2013). Within the exposed volcanic centres the Börzsöny and Visegrád Mts. have to be mentioned, since they were active from 16.5 to 13.5 Ma (Karátson et al. 2000, 2007). In the Vienna Basin volcanic centres are missing, and only rare tuff horizons were described at the base of the Jakubov Fm. (Sant et al. in press).

Methods

Sedimentology and paleobotany

The outcrop was manually excavated to expose the full section in the forest scour. To provide more insight, the section was cleaned by palette knifes and brushes. The lithofacies abbreviations were modified from Németh & Martin (2007) and Miall (2006). Leaves were described using the current terminology published by Ash et al. (1999) and Ellis et al. (2009).

Petrology and chemistry

For grain-size analysis thin sections were used, and grain dimensions were measured by metric scale. Measurements of fine vitroclasts were not possible due to alteration. Therefore only grains above 0.25 mm were labelled and their percentage was determined by image analysis using QuickPHOTO-MICRO 3.1 (Comenius University in Bratislava). Image analysis of macro samples was used for determination of the lapilly content. Mineral composition was analyzed under polarizing microscope and under the Cameca SX 100 microprobe (State Geological Institute of Dionýz Štúr). Minerals were measured using WDS analysis with accelerating voltage 15 keV, probe current 20 nA with a beam width of 10 μm. The beam width of 2 μm was used on microlitic minerals in lithoclasts. All vitroclasts were measured under 2 conditions: probe current 3 nA (Na, K, Si) and 10 nA (other elements) for elimination of mobile element loss. Raw analyses were recalculated to weight percent of oxide using the ZAF correction. Other minerals were determined by EDAX analyses. Four whole rocks samples were selected from different levels of the section (Fig. 2). Samples were send to Bureau Veritas mineral laboratories (Canada, Vancouver). Samples were pulverized and prepared for analysis by Lithium Borate Fusion. Major elements were analyzed by ICP-ES, and trace elements by ICP-MS. X-ray analysis was performed by using the Bruker D8 Advance (Earth Science Institute of SAS), with measurement parameters: CuKα radiation generated by 40 kV and 40 mA, iris: 0.3°–6 mm–0.2062°, primary and secondary Sollers iris: 2.5°; step: ≈0.02 °2θ; time/step: 1.25 and 0.8 s, interval: 2–65 °2θ. Diffracted radiation was sensed by a positionally sensitive detector SSD 160 working in 1D regime. Powdered whole rock samples and oriented slides from <2 and <0.2 μm fractions were analyzed. Separation was done according to Jackson (1975). Oriented slides were analyzed in two states: natural state (Ca form) and following an ethylene glycol saturation (8 hours at 60 °C).

$^{40}Ar/^{39}Ar$ dating

Approximately a 2 kg ash sample was processed at the Mineral Separation facility of the Earth Sciences Department at the VU University Amsterdam to separate sanidine and biotite from the Kuchyňa tuff for $^{40}Ar/^{39}Ar$ dating. First, the sample was crushed into ~1 cm^3 pieces, disintegrated in a diluted calgon solution with a Robot Coupe blixer 4 v.v., treated in an ultrasonic bath, and wet sieved into a fraction between 150 and 500 μm. K-feldspar (sanidine) grains were isolated from the 2.54–2.59 g/cm^3 density fraction (using di-iodomethane) and further purified by using magnetic separation over the Frantz isodynamic separator and cleaned by a 10 minute ultrasonic HNO_3 bath (subsequently rinsed with distilled water). The most transparent, inclusion free sanidine grains from the 250–500 μm fraction were handpicked under an optical microscope. Biotite was extracted from the density fraction >3.00 g/cm^3 and cleaned in an ultrasonic bath. The thickest, most angular hexagonal biotite crystals without visible inclusions were handpicked under an optical microscope in the 200–400 μm fraction.

The selected mineral separates were packed in 6 mm ID AI packages, loaded together with Fish Canyon Tuff sanidine (FCs) standards in 25 mm ID Al cups and irradiated at the Oregon State University TRIGA reactor in the cadmium shielded CLICIT facility for 18 hours (irradiation code VU107). $^{40}Ar/^{39}Ar$ analyses were then carried out at the geochronology laboratory of the VU University, Amsterdam, on an ARGUS VI$^+$ noble gas mass spectrometer.

Single grain fusions were performed on 17 sanidine grains and 5 biotite grains in June 2017. Ages are calculated with Min et al. (2000) decay constants, atmospheric air value 298.56 (Lee et al. 2006) and 28.201±0.022 Ma for FCs (Kuiper et al. 2008). The correction factors for neutron interference reactions are $(2.64\pm0.02)\times10^{-4}$ for $(^{36}Ar/^{37}Ar)_{Ca}$, $(6.73\pm0.04)\times10^{-4}$ for $(^{39}Ar/^{37}Ar)_{Ca}$, $(1.21\pm0.003)\times10^{-2}$ for $(^{38}Ar/^{39}Ar)_K$ and $(8.6\pm0.7)\times10^{-4}$ for $(^{40}Ar/^{39}Ar)_K$. Data analysis and age calculations were performed in ArArCalc software (Koppers 2002). All errors are quoted at the 2σ level and include all analytical errors. All relevant analytical data for age calculations can be found in the online supplementary material.

FT dating

A 5 kg rock sample was crushed and sieved (<315 μm). Apatite and zircon mineral concentrates were produced using

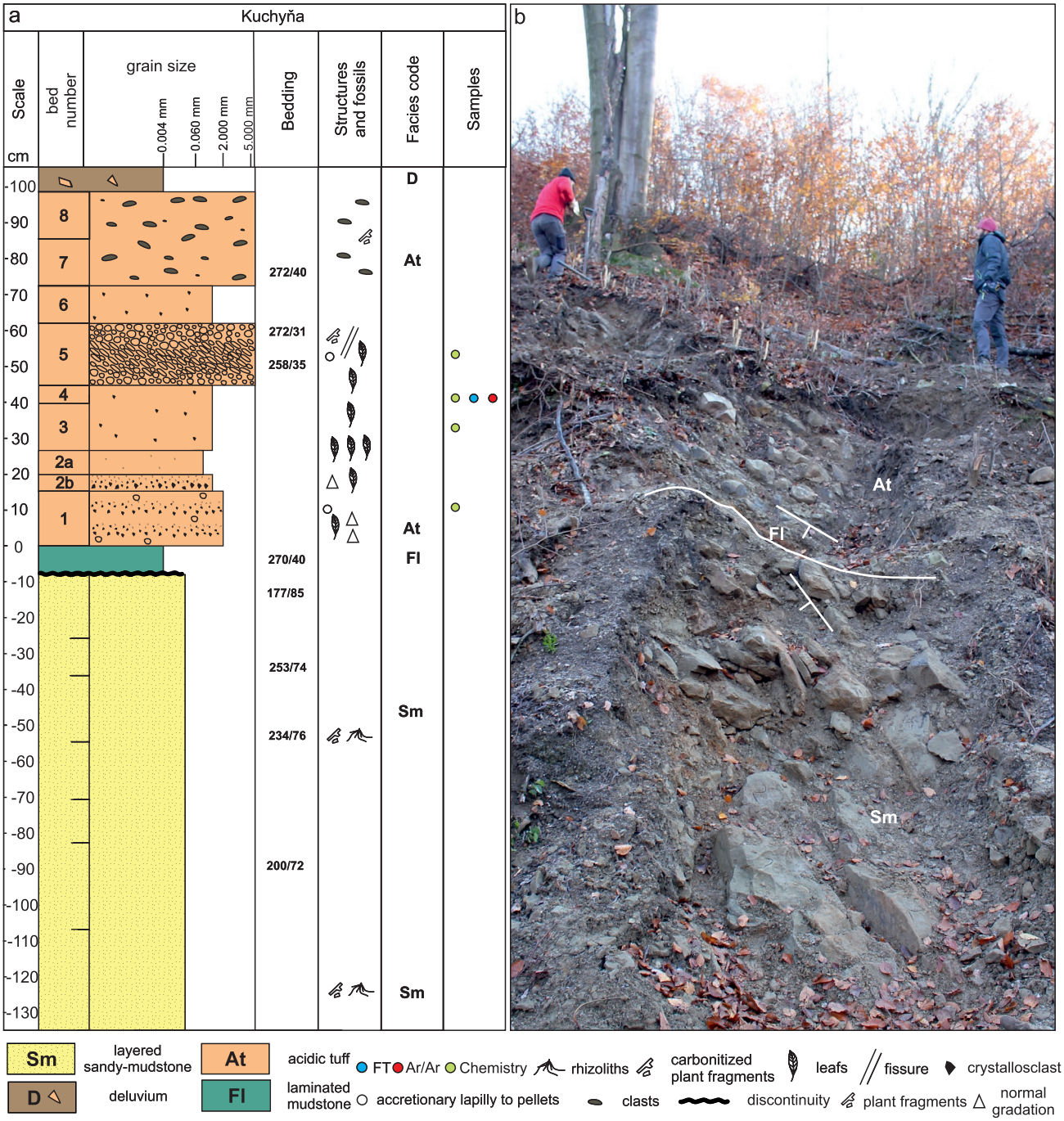

Fig. 2. a — Lithological column of the studied section; **b** — studied outcrop. The white line indicates the base of the tuff. The white T shaped lines highlight the angular contact.

the Wilfley table, a Frantz magnetic separator and conventional heavy liquid methods. Handpicking under an optical microscope was the final stage for apatite and zircon separation to provide pure concentrates. Final sample preparation and analysis of fission track (FT) samples was carried out at the University of Innsbruck. Mineral separates were mounted in epoxy resin (apatite) and PFA®Teflon (zircon) was ground, and polished with a series of polishing papers going from 1200, 1000, 9, 6 and 3 μm to provide a clear surface. Apatites for age determination were etched for 40 seconds at 21 °C with 6.5 % nitric acid; zircon mounts 3–6 h at 235 °C in a NaOH–KOH eutectic melt to reveal spontaneous tracks (Fleischer & Price 1964). Two U-free muscovite detectors were sealed against the polished and etched surfaces (external detector method; Gleadow & Duddy 1981).

For irradiation the samples were sent to the FRM II research reactor in Garching, Germany. Two dosimeter glasses of known uranium content, CN1 (for zircon) and CN5 (for

apatite), were included to determine the neutron flux during irradiation (Hurford & Green 1983). After irradiation, the external mica detectors of samples and dosimeter glasses were etched in 40 % hydrofluoric acid at 21 °C for 40 minutes. Tracks in apatites, zircons, and mica detectors were counted using a Zeiss Axio Imager A1m microscope equipped with an AUTOSCAN stage (analyst: M. Reiser). FT ages were determined using the Zeta calibration approach (Hurford & Green 1983), with ζ=318±27 for apatite (dosimeter glass CN-5) and ζ=130±10 for zircon (CN-1 dosimeter). They are reported as central ages (Galbraith & Laslett 1993) with a 1σ error. FT etch-pit diameters (Dpar) were measured to estimate the compositional influence on fission-track annealing (Carlson et al. 1999). Ages were calculated using the TRACKKEY program, version 4.2.g (Dunkl 2002). A central age is given for samples that pass the Chi-square test (P>5 %; Galbraith 1981). The partial annealing zone for apatite FT (APAZ) ranges from 60 to 120 °C (e.g., Green et al. 1986; Green & Duddy 1989; Gallagher et al. 1998) with a mean effective closure temperature of 110±10°C (Gleadow & Duddy 1981). For the interpretation of zircon FT data, this study used a zircon partial annealing zone (ZPAZ) between 200 and 300 °C (cf. Tagami & O'Sullivan 2005).

Results

Sedimentology

The Kuchyňa section starts with thinly laminated or massive, muddy sandstones of pale brown to yellow colour (Figs. 2, 3). No signs of traction transport were observed. The content of rhizoids and wood fragments is high, but leaves are not present in this level. Moreover, no marine, brackish or fresh water macrofauna was found. Foraminifers and calcareous nanofossils are also absent and the sediments show no signs of bioturbation. A brick-red to brown coloured, ~8 cm thick clay layer is present on top of the sandy mudstones (Fig. 3f). above an angular contact between the muddy sandstones and tuffs is observed. The muddy sandstones show an average strike of 216° and dip of 78° and the overlying tuff layers display an average strike of 267° and dip of 36.5°.

The total tuff thickness reaches ~97 cm which is more than the formerly measured 30 cm (Šimon et al. 2009). The tuff is overlain by recent soil and by deluvial muddy conglomerate, so the total thickness of this tuff might probably be even larger. Spherical weathering (exfoliation) has been observed. In a few cases the tuff is cut by fissures filled with reddish mudstone. These discontinuities seem to be almost perpendicular to the bedding planes. A specific feature of the Kuchyňa tuff is the high abundance of leaves and wood fragments, which are more than 12.5 cm long.

The tuff consists of at least eight discontinuous parallel beds with no interbeds of non-volcanic material. Due to the poor preservation and high degree of fragmentation, description of structures is difficult. The thickness of the individual tuff beds ranges from 5 to 20 cm. The lowermost tuff bed contains two visibly graded intervals (1–2 cm thick), which range from coarse to medium grained ash based on visually observed grain size characteristics. Rare accretionary lapilli have been observed. The second bed shows gradation and abundant leaves. The bed starts with coarse grained ash and passes to fine grained ash. The following beds are composed of massive medium to fine grained ash with abundant leaves at the lower bed boundary. The leaves also occur within the bed and are often plastically deformed. The next bed yields matrix to clast supported accretionary lapilli (Fig. 2 n.5; Fig. 3). The accretionary lapilli are often poorly recognizable macroscopically, especially in dry samples. They are composed of internally massive ash aggregates with a thin finer-grained outer rim (Fig. 3a,b,d). Based on their structure they can be defined as coated ash pellets or accretionary pellets (after Thordarson 2004; modified by Brown et al. 2010, 2012). The lapilli are often elliptical in shape and 3–6 mm long (rarely up to 16 mm long; Fig. 3b,d). They are deformed in the central part of the layer, while the base and top of the bed yield undeformed lapilli. These deformed lapilli highlight a plastic deformation of the bed (Fig. 3d). The bed is cut by fissures filled with sandy grains. A massive medium to fine grained ash bed follows. The section ends with layers that yield abundant admixture of rounded non-volcanic granule to pebble size clasts and plant fragments (Fig. 2 n.6–8; Fig. 3c).

The fossil leave association originally described by Fordinál et al. (2010) is completed by newly discovered species like: *Quercus* cf. *drymeia* and *Trigonobalanopsis rhamnoides*.

Petrography

The Kuchyňa tuff layers can be microscopically described as crystallo–vitroclastic tuff with a little admixture of non-volcanic lithoclasts. The basal tuff layers contain 8.7–13 % particles above 0.25 mm in size (Table 1), which mostly consist of pumice fragments. The following layers are composed of fine tuffs (97–99 % of the clasts are smaller than 0.25 mm). About 50 cm above the red clay layer a lapilly tuff with 29–38 % of accretionary lapilli occurs (Fig. 2). This layer is covered by a fine tuff (97 % of the clasts are under 0.25 mm). In the upper part (85 cm and higher), the fine tuffs contain admixture of ca. 5 % of nonvolcanic lithic clasts, which are often larger than 2 mm in diameter.

Pumice fragments and glass shards are dominant in the tuff composition (Fig. 4). The vitroclasts can be divided into two types. One type is composed of volcanic glass with rough boundaries. These volcanic glass shards of rhyolitic composition (Table 2, Fig. 5b) are often vesiculated or Y-shaped and form the majority of the vitroclasts. However, the total sum of oxides is low (92 wt. %; Table 2) and indicates alteration. The very fine particles and highly vesiculated pumice fragments were altered into clay minerals. The remaining vitroclasts are less frequent, microlithic and slightly altered (Fig. 4a–b).

Fig. 3. Outcrop pictures: **a** — detail of the tuff layer with accretionary lapilli; **b** — tuff layer with deformed accretionary lapilli; **c** — tuff layer with lithoclasts; **d** — synsedimentary folded accretionary lapilli, the black dashed line marks the presumed folding; **e** — contact layer between sandy mudstones and the Kuchyňa tuff, also note the exfoliation in the tuff; **f** — detail onto individual layers of the section; **g** — underlying sandy mudstone with rhizoliths. For other abbreviations see Fig. 2.

Table 1: Grain size composition of the Kuchyňa tuff and modal analysis of clasts larger than 0.25 mm in diameter.

Depth (cm over tuff base)	10	20	25	40	70	85	95	45–60
Layer	n.1	n.2b	n.2a	n.3–4	n.6	n.7	n.8	n.5*
Fraction (mm)	%	%	%	%	%	%	%	%
>2						4.34	1.64	29–38
1–2	2.02					0.19	1.98	
0.5–1	3.68	2.76	0.19	0.70	0.52	0.43	2.34	
0.25–0.5	2.98	10.40	0.60	2.24	2.24	2.84	1.75	
<0.25	91.32	86.85	99.20	97.06	97.25	92.19	92.30	61–71
Grains above 0.25 mm (%)	*8.68*	*13.16*	*0.79*	*2.94*	*2.76*	*7.80*	*7.71*	acc.
Vitroclasts & pumice	6.43	10.42	0.66	1.94	1.77	2.32	1.66	lapilli
Crystalloclasts	2.00	2.41	0.13	0.83	0.56	0.80	0.53	
Lithoclasts	0.25	0.33	0.00	0.17	0.43	4.68	5.52	

The crystalloclasts are composed of plagioclase, sanidine, biotite, amphibole, quartz and small amounts of pyroxene, apatite, zircon, rutile and rare monazite. Some crystalloclasts with remnants of adhering glass have been found (Fig. 4a). Crystalloclasts do not show zonality and their shape is hypidiomorphic with marks of fragmentation in the solid state. Among the feldspars, plagioclase crystalloclasts are dominant and sanidine is less frequent. The chemical composition of plagioclase varies in the range $An_{37–52}$, but a crystalloclast of An_{79} was also found (Table 3, Fig. 6a). The chemical composition of sanidine crystalloclasts and composition of sanidine crystals with adhering volcanic glass (Fig. 4a) varies from $Or_{62–65}$ to $Or_{73–74}$ (Table 4, Fig. 6a). In addition, all sanidine crystalloclasts contain 0.022–0.039 apfu of Ba. Amphibole crystalloclasts are green to brown-green in colour and relatively small. They are pargasite to magnesio-horblende in composition (Table 5, Fig. 6b). Long, tabular biotites are annite in composition (Table 5). Decay along cleavage planes is documented by thin zones of different colours in the BSE image (Fig. 4c). Some biotite crystalloclasts are bent and/or frayed. Beside relatively fresh and large biotites, some altered sagenitic biotite and sagenitic textures have also been observed. However, based on the presence of non-volcanic lithoclasts composed of quartz (Qz) and altered biotite (Bt) with sagenite inclusions (Bt paragneiss), these sagenitized biotites are interpreted as non-volcanic in origin. Both orthopyroxene (enstatite) and clinopyroxene (augite) crystalloclasts (Table 5) are also present. The rest of adhering microlithic groundmass on the edge of an Opx crystalloclast (Fig. 4d) is formed by plagioclase with An_{63}, Opx and ilmenite. However, opx microliths did not reach the size required for the probe measurement. The volcanic lithoclasts are extremely rare, due to the fine grain size of the tuff.

The non-volcanic lithoclasts without any thermal effect are composed of biotite paragneiss (Fig. 7a), cherts/felsites, low-grade metapelites such as Qz–mica shale/phyllite (Fig. 7b), carbonate shale and rare sandstones. The metasediment clasts contain zircon, quartz, albite and mica (Fig. 4f). Polycrystalline quartz is also non-volcanic in origin. Given the purpose of the paper, a lithoclast composed of quartz, biotite, monazite and feldspar was also analyzed (Fig. 4e). The feldspar composition in the lithoclasts is between sanidine and anorthoclase (Fig. 6a) and they do not contain Ba (Table 4). However, these feldspars are around 15 μm in size and, therefore, could not affect the $^{40}Ar/^{39}Ar$ dating (Fig. 4e).

The Kuchyňa tuff also contains clay minerals as products of alteration of glass. X-ray analysis documented a large portion of amorphous volcanic glass, which is characterized by wide diffusion reflex between 16 to 30 °2θ. In both clay fractions smectite dominates (Fig. 7c). Values d(060)=1.4969 Å are characteristic for dioctahedral forms of smectite. The chemical composition of the clays best corresponds to montmorillonite, but the sum of oxide is very low (Table 2). Moreover, halloysite was also identified. Powdered, whole rock samples confirmed the presence of smectite, plagioclase, biotite, quartz, crystobalite and ilmentite.

Due to alteration, the whole rock chemical composition is influenced by alkali loss. So it must be interpreted carefully mainly in regard to the major oxides. Based on whole rock analyses, the Kuchyňa tuff belongs to the calc–alkaline series of the peraluminous type. The Zr/Y ratio (7.5–10.3; Table 2) also indicates affinity to the calc–alkaline series (Barret & MacLean 1994). Based on the TAS diagram (Le Bas et al. 1986) the tuff is rhyolite to dacite in composition (Fig. 5b, Table 2). However, a high content of volatile components (LOI 13.9–9.3 %) and alteration to clay mineral excludes the use of the TAS diagram. Samples are displayed in a classification diagram based on trace elements (Pearce 1996; Fig. 5a) in the trachyte to rhyolite/dacite field. The CIPW calculation (Table 6) also indicates rhyolitic composition. Discrimination based on Co–Th (Fig. 5c; Hastie et al. 2007), and $K_2O–SiO_2$ (Fig. 5d; Peccerillo & Taylor 1976) indicates rhyodacite rocks of high-K calc–alkaline series. The Kuchyňa tuff shows an Eu anomaly of 0.59, high LREE content (Table 2), depletion in P, Nb, Ta, Ti and enrichment in Pb (Fig. 5e,f). The Eu anomaly of 0.59 indicates plagioclase fractionation during magma evolution. The LREE/HREE ratio indicates a possible garnet fractionation.

$^{40}Ar/^{39}Ar$ dating results

The majority of single grain fusion feldspar measurements yield high radiogenic ^{40}Ar values (>90 % $^{40}Ar^*$), and, thus, relatively low amounts of atmospheric ^{36}Ar, indicating a minimal impact of potential alteration of the dated mineral (ESM. 1). The ^{37}Ar values are for most samples between 0.3 and 2.2 fA. High ^{37}Ar values reflect high Ca-content pointing to plagioclase instead of sanidine (K-feldspar). Plagioclase can result in lower quality age determinations than sanidine because of its low K content. Incorporation of excess argon will have large effects on the measurements and may result in overestimated ages (McDougall & Harrison 1999). Moreover, neutron interference corrections are more substantial for plagioclase (due

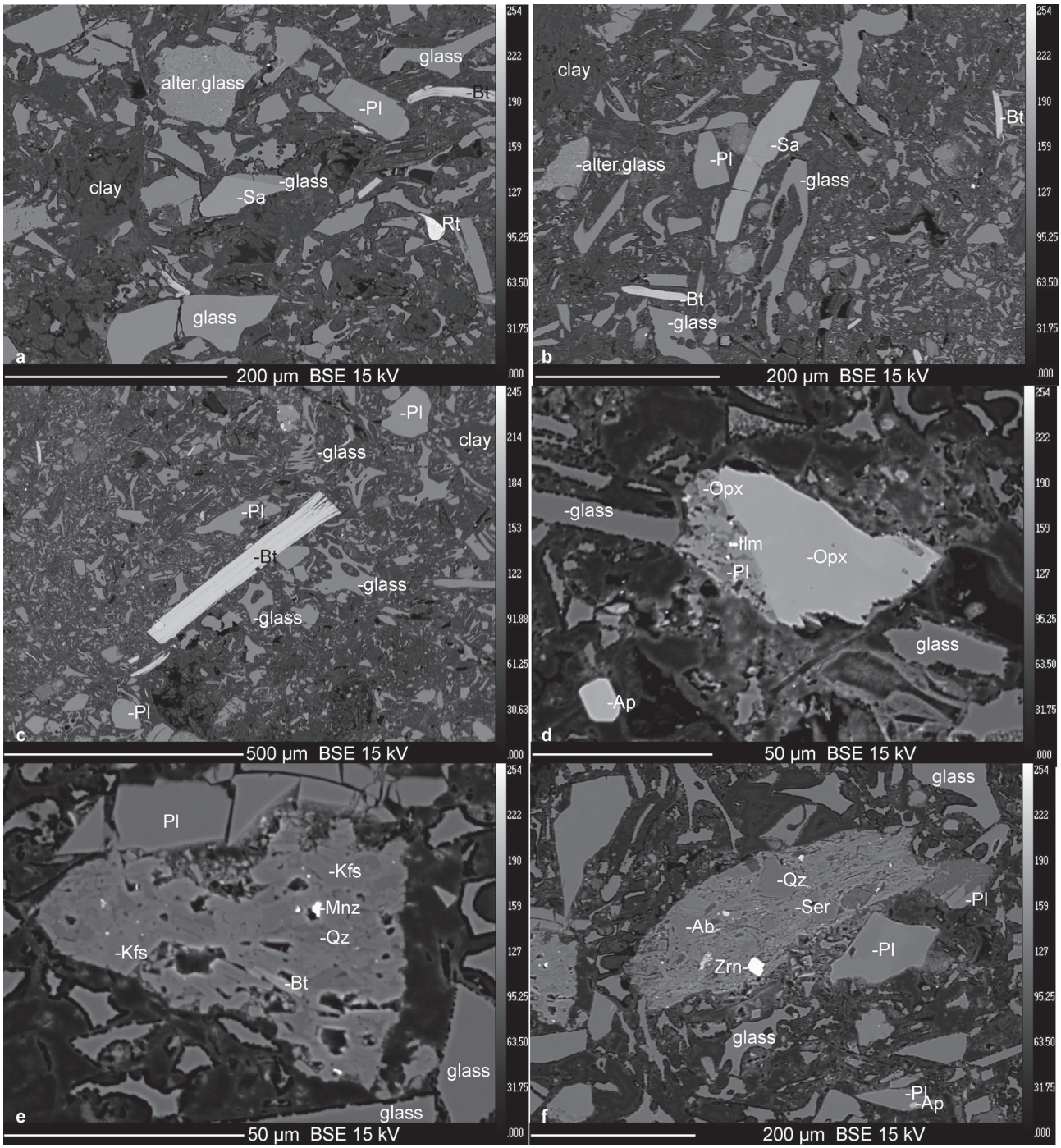

Fig. 4. Kuchyňa tuffs in BSE images: **a** — crystalloclast of sanidine with adhering glass (analysis 4 core, analysis 5 rim); **b** — sanidine crystalloclast (analysis 1 core, analysis 2 rim); **c** — biotite crystalloclast (analysis 22); **d** — orthopyroxene crystalloclast (analysis 31) with adhering microlithic glass; **e** — granitoid/gneiss lithoclast composed of Kfs (analysis 6+7), Qz, Bt and Mnz; **f** — metapelite lithoclast composed of Ab, Qz, Ser and Zr.

to the ^{40}Ca (n, nα)^{36}Ar and ^{42}Ca(n,α), ^{39}Ar reactions during irradiation) yielding larger analytical uncertainties (McDougall & Harrison 1999). Therefore, only the most reliable grains with ^{40}Ar >90 % and ^{37}Ar <1.5 fA are considered for the age determination. These generally yield the highest measured values of ^{40}Ar. The weighted mean age (assumed to be the age of the volcanic eruption) is based on the youngest grains that define a plateau and the data are included as long as the mean weighted standard deviation (MWSD) is <statistical T-test at a confidence level of p5 %. The mean weighted age is 15.23±0.04 Ma (n=3; Fig. 8). The full range of the reliable sanidine grains is 15.22±0.02 Ma to 15.40±0.01 Ma.

The small set (n=5) of single grain biotite measurements is characterized by low ^{40}Ar* values, pointing to alteration for

Table 2: Whole rock chemical composition of tuffs together with probe analysis of glass shards and indicative probe analyses of clay matrix *****Fe_2O_3, was recalculated from FeO. Clay minerals were normalized to 44 total cation charges, to balance $O_{20}(OH)_4$ and all Fe was considered as Fe^{3+}. Analyses of clay minerals must be taken as informative, because the thin sections were not prepared and measured with respect to clay minerals.

Analyse		Whole rock				Glass shards								Clay		
Sample		n-1	n-3	n-4	n-5	anal.	38	39	1/19	2/19	3/19	4/19	5/19	anal.	40	41
SiO_2	%	56.68	59.21	65.12	64.08	SiO_2	71.38	71.78	72.94	73.23	72.14	72.72	69.31	SiO_2	27.56	28.09
TiO_2		0.25	0.15	0.12	0.23	TiO_2	0.05	0.06	0.09	0.08	0.02	0.06	0.06	TiO_2	0.05	0.04
Al_2O_3		18.12	17.00	14.55	15.52	Al_2O_3	11.64	11.49	11.59	11.55	11.76	11.44	12.05	Al_2O_3	12.85	13.92
Fe_2O_3		3.22	2.93	2.77	2.44	FeO	0.65	0.86	1.03	0.99	0.72	0.96	0.81	*Fe_2O_3	*1.38	*1.44
Cr_2O_3		n.d.	n.d.	n.d.	0.002	Cr_2O_3	0.00	0.00	0.00	0.01	0.01	0.00	0.00	Cr_2O_3	0.02	0.02
MgO		2.04	1.57	1.42	1.36	MgO	0.01	0.03	0.06	0.07	0.06	0.08	0.04	MgO	0.48	0.78
MnO		0.05	0.05	0.04	0.04	MnO	0.06	0.05	0.12	0.04	0.00	0.00	0.10	MnO	0.00	0.00
CaO		2.34	1.56	1.52	1.80	CaO	0.64	0.80	1.01	1.05	0.77	0.98	0.80	NiO	0.02	0.00
Na_2O		1.35	1.25	1.34	1.59	NiO	0.00	0.01	0.00	0.01	0.03	0.01	0.00	CaO	0.61	0.62
K_2O		1.78	2.49	3.40	3.43	Na_2O	2.94	3.32	3.07	3.03	2.99	3.13	3.33	K_2O	0.11	0.14
P_2O_5		0.06	0.03	0.03	0.06	K_2O	4.70	4.30	3.89	4.19	4.76	4.04	4.50	Na_2O	0.02	0.05
LOI		13.9	13.6	9.5	9.3	P_2O_5	0.00	0.01	0.00	0.03	0.02	0.02	0.04	Cl	0.56	0.51
sum		99.89	99.92	99.81	99.85	SO_3	0.00	0.00	0.01	0.00	0.00	0.02	0.00	F	0.00	0.00
C_{tot}		0.22	0.18	0.02	0.17	Cl	0.07	0.05	0.10	0.10	0.10	0.09	0.09	*Tot*	43.66	45.61
S_{tot}		n.d.	n.d.	n.d.	n.d.	Tot	92.14	92.75	*93.93*	*94.39*	*93.37*	*93.56*	*91.13*	Si	7.536	7.365
Sc	ppm	5	3	3	4	Tot-Cl	92.13	92.74	93.90	94.36	93.35	93.54	91.11	^{T}Al	0.464	0.635
Ba		759	908	788	693									Sum	8.000	8.000
Co		2.8	2.6	3.6	2.3									Al	3.677	3.664
Cs		3.7	3.6	4	5									Ti	0.011	0.008
Ga		18.0	16.2	15.4	14.8									Fe^{3+}	0.189	0.190
Hf		5.1	4.3	3.7	4.3									Mg	0.195	0.304
Nb		17.9	16.2	14.5	14.4									Mn	0.000	0.000
Rb		70.3	76.2	104.3	106.8									Cr	0.004	0.004
Sr		125.7	81.5	89.2	105.7									Ni	0.004	0.000
Ta		1.6	2.0	1.6	1.4									sum	4.082	4.171
Th		23.2	23.6	18.9	18.2									Ca	0.178	0.175
U		2.4	3.5	4.1	4.1									K	0.040	0.047
V		21	15	9	21									Na	0.012	0.023
Zr		175.1	125.4	114.0	132.4									sum	0.230	0.245
Y		16.9	14.4	13.9	17.7											
La		37.7	27.2	26.8	34.3											
Ce		68.0	51.2	43.7	56.5											
Pr		6.81	5.01	5.30	6.43											
Nd		22.4	16.2	18.0	20.9											
Sm		3.79	2.89	3.06	3.76											
Eu		0.72	0.51	0.54	0.70											
Gd		3.07	2.47	2.56	3.45											
Tb		0.49	0.39	0.43	0.54											
Dy		2.94	2.22	2.68	3.15											
Ho		0.53	0.47	0.49	0.64											
Er		1.63	1.35	1.67	1.97											
Tm		0.25	0.21	0.23	0.31											
Yb		1.65	1.48	1.57	2.18											
Lu		0.27	0.23	0.29	0.33											
Eu/Eu*		0.645	0.584	0.588	0.592											
La/Yb		16.39	13.18	11.60	10.69											
Zr/Y		10.36	8.71	8.20	7.48											

most of the samples. Moreover, they generally yielded lower beam intensities (<90 fA) of ^{40}Ar than the Kuchyna tuff, so the results are less precise. The most reliable biotite analysis (067_VU107) with ^{40}Ar* of 74 % yields an age of 15.05± 0.12 Ma, and might be close to the eruption age (Fig. 8).

FT results

The measured apatite grains are predominantly tabular and prismatic crystals or crystal fragments. D_{par} (average etch pit diameter) measurements indicate a fluorine dominated apatite composition (D_{par}<2.0 μm). Presence of fluorapatite was also confirmed by the microprobe (Table 5). However, no correlation between age and composition has been observed. Based on mesurement of 24 grains an age of 14.5±2.8 Ma was obtained (Table 7). It should be noted that several grains exhibit very low track densities (average Ns<2 per grain). After including these grains in the calculation the resulting ages will be younger (12.1±2.3 Ma; Table 7). Zircon FT analyses based on 15 grains yields a central age of 13.7±1.2 Ma (Table 7). Controversially to their respective closure temperatures, the zircon age is younger than the apatite age, but they still overlap within their respective error bars.

Discussion

Age of the Kuchyňa tuff

The juvenile origin of sanidine is documented by the presence of adhering glass on the rim of the crystalloclasts (Fig. 4a). The 15.23±0.04 Ma plateau age of sanidine is in accordance with the assignment of the Devínska Nová Ves Fm. to the middle Badenian (Langhian; Fordinál et al. 2010,

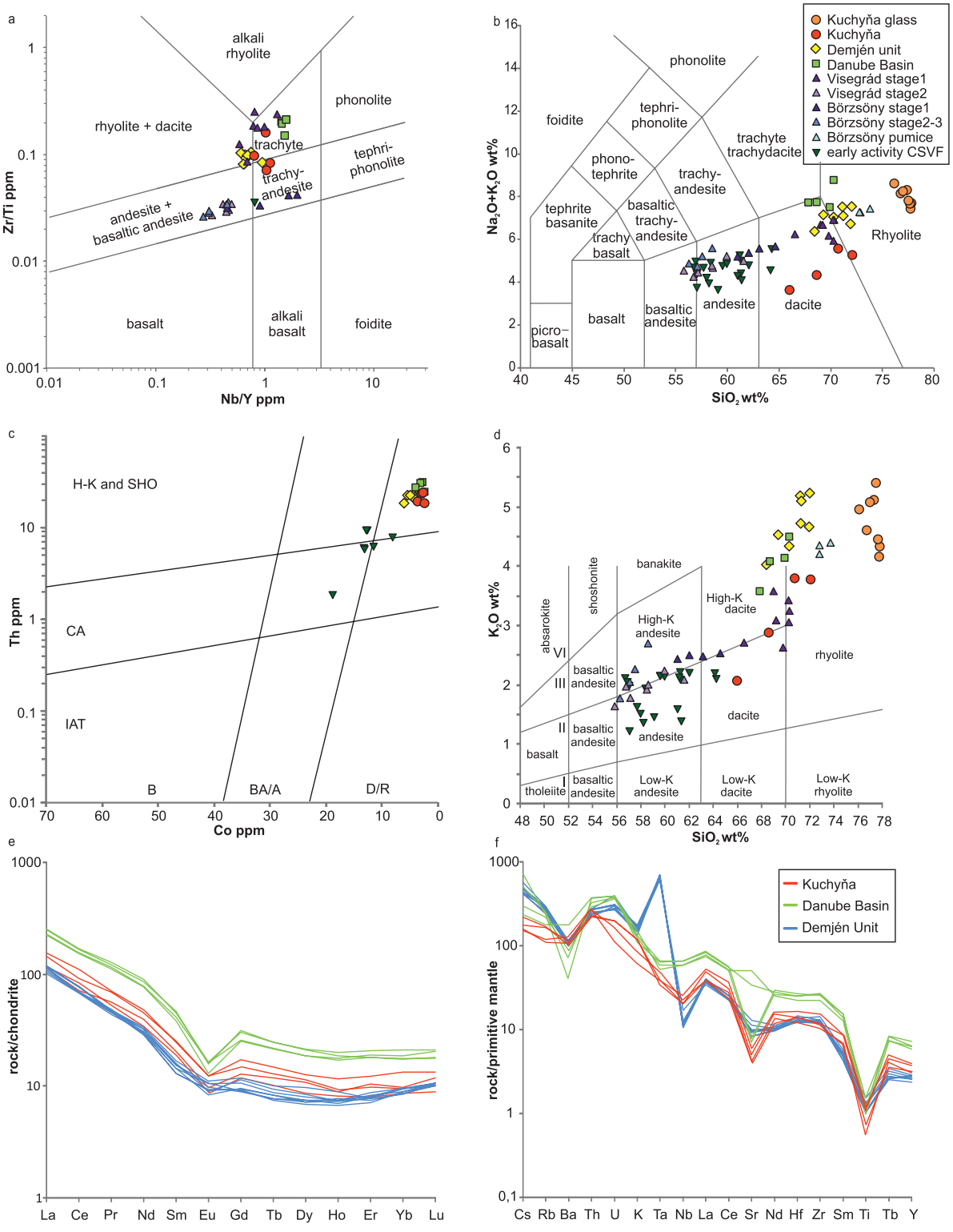

Fig. 5. Chemical composition of the Kuchyňa tuff. Note that the major element diagrams are only illustrative, because of the low oxide sum in the Kuchyňa tuff (see Table 2). Analyses were recalculated to 100 % free of volatiles before plotting in b and d diagrams. Comparative samples taken from: Börzsöny–Visegrád region — Harangi et al. 1995; Karátson et al. 2000, 2007; Demjén Unit — Lukács et al. 2018; CSVF (Central Slovak volcanic field) — Harangi et al. 1995; Konečný et al. 1995, 1998; Chernyshev et al. 2013; Danube Basin — Šarinová (personal data from tuffs occurring within the NN5 zone). **a** — Pearce (1996) diagram; **b** — TAS diagram (Le Bas et al. 1986); **c** — discrimination based on Co–Th (Hastie et al. 2007), IAT — island arc tholeiite; CA — calc–alkaline; H-K — high-K calc–alkaline; SHO — shoshonite; **d** — discrimination based on major oxides (Peccerillo & Taylor 1976), I: tholeiite series, II: calc-alkaline series, III: high-K calc–alkaline series, IV: shoshonite series; **e** — Chondrite-normalized REE distribution (after McDonough & Sun 1995); **f** — primitive mantle-normalized multi-element diagram (normalizing values after Sun & McDonough 1989).

2012a; Polák et al. 2012) or to the early Badenian sense Kováč et al. (2007, 2018; Fig. 1c).

The results of AFT data are put in question due to the presence of apatites with no tracks (Table 7). If the age value gained from apatites without tracks is excluded, the AFT indicates an age of 14.5±2.8 Ma. This is roughly consistent with the sanidine age data, taking into account the error bars. However, zircon FT analyses yielded an age of 13.7±1.2 Ma which is younger than the $^{40}Ar/^{39}Ar$ sanidine age. The younger zircon age cannot be interpreted as a later thermal overprint because the closing temperature for zircon FT is higher than the closing temperature for apatite FT and sanidine. The small number of the measured zircon grains may account for the larger errors in the results.

These results are not fully compatible. But, if the sanidine is really juvenile, the Ar/Ar single grain age data are prioritized. Additionally, a tuffite horizon overlaid by the Jakubov Fm. (younger than 14.6 Ma based on *Orbulina suturalis*) was found in the Bernhardsthal-4 well, in the NE Vienna Basin (Sant et al. in press). Based on Ar/Ar dating of biotite, the tuffite from Bernhardsthal-4 well yields an age range of ~15–16 Ma, what is in accordance with the age of the Kuchyňa tuff. Other supporting argument for the middle Miocene age is the occurrence of *Trigonobalanopsis rhamnoides*. Since *Trigonobalanopsis rhamnoides* is absent in the late Miocene of the northern parts of the Paratethys region (Kovar-Eder & Hably 2006), the presence of the taxon indicates a close relation to the early and middle Miocene plant record in the Paratethys realm. The tuff age points to the fact that the Badenian transgression did not reach the area sooner than around 15 Ma, what is in accordance with the general setting for this region (e.g., Sant et al. 2017).

Table 3: Composition of plagioclase. Chemical composition was calculated based on 8 oxygens.

Analyse	3	17	18	19	20	21	36
Comment	clast	clast	clast	clast	clast	clast	microlith
SiO_2	56.73	57.12	59.15	47.38	55.06	55.20	54.47
Al_2O_3	27.31	26.50	25.22	33.32	28.03	27.47	27.72
SrO	0.09	0.05	0.03	0.08	0.09	0.09	0.04
FeO	0.18	0.24	0.27	0.23	0.38	0.24	0.90
MgO	0.00	0.00	0.00	0.00	0.02	0.00	0.37
CaO	9.61	9.04	7.75	16.61	10.81	9.88	11.96
Na_2O	6.13	6.21	6.85	2.26	5.21	5.69	3.63
K_2O	0.32	0.36	0.51	0.08	0.31	0.33	0.35
Total	*100.36*	*99.52*	*99.78*	*99.94*	*99.90*	*98.90*	*99.45*
Si	2.544	2.578	2.652	2.179	2.490	2.516	2.478
Al	1.443	1.410	1.333	1.806	1.494	1.476	1.486
Sr	0.002	0.001	0.001	0.002	0.002	0.002	0.001
Fe	0.007	0.009	0.010	0.009	0.014	0.009	0.034
Mg	0.000	0.000	0.000	0.000	0.001	0.000	0.025
Ca	0.462	0.437	0.372	0.818	0.524	0.482	0.583
Na	0.533	0.543	0.596	0.202	0.457	0.503	0.320
K	0.019	0.021	0.029	0.005	0.018	0.019	0.020
Cat sum	*5.010*	*4.999*	*4.994*	*5.021*	*5.000*	*5.007*	*4.949*
Or %	1.83	2.05	2.95	0.44	1.77	1.89	2.22
Ab %	52.61	54.28	59.74	19.69	45.76	50.09	34.66
An %	45.56	43.67	37.32	79.87	52.47	48.01	63.12

Depositional setting

Based on the floral assemblages determined by Fordinál et al. (2010) together with the new findings of this work, it is possible to interpret climatic conditions during the time of tuff deposition. Fossil leaves of *Quercus* cf. *drymeia*, Lauraceae gen. et sp. indet., *Trigonobalanopsis rhamnoides* document subtropical, humid continental conditions with hinterland and lowland evergreen broadleaved forests. The presence of

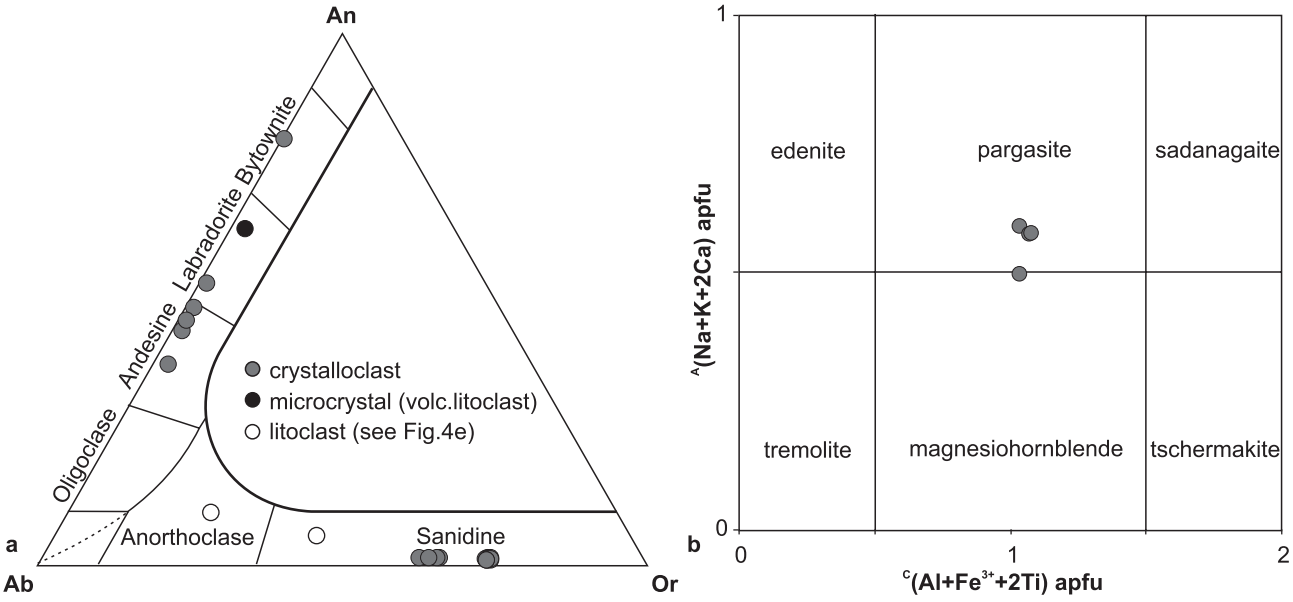

Fig. 6. a — Feldspar classification diagram; **b** — Amphibole classification diagrams (Hawthorne et al. 2012).

Table 4: Composition of K-feldspar. Chemical composition was calculated based on 8 oxygens.

Analyse	1	2	4	5	8	9	10	11	12	13	14	15	16	6	7
N. crystal	1core	1rim	2core	2rim	3core	3rim	4	5	6	7	8	9	10	11	12
Position	clast	clast	clast	clast	clast	clast	clast	clast	clast	clast	clast	clast	clast	lithoclast	lithoclast
SiO_2	64.05	64.21	64.73	64.56	64.09	64.30	64.51	65.19	64.12	64.14	65.17	64.69	64.17	66.55	66.33
Al_2O_3	20.47	20.11	20.43	20.64	20.23	20.12	20.34	20.33	20.47	20.45	20.41	20.47	20.28	20.82	21.77
FeO	0.10	0.13	0.13	0.10	0.11	0.13	0.27	0.08	0.05	0.12	0.14	0.11	0.11	0.17	0.19
MgO	0.01	0.00	0.00	0.00	0.00	0.00	0.00	0.00	0.00	0.00	0.00	0.00	0.01	0.03	0.00
BaO	2.13	2.10	1.37	1.30	1.88	2.02	1.53	1.22	2.16	2.14	1.76	1.27	1.87	0.15	0.15
CaO	0.14	0.15	0.19	0.22	0.15	0.16	0.14	0.23	0.17	0.19	0.20	0.15	0.18	1.05	1.98
Na_2O	2.78	2.77	3.93	4.03	2.68	2.77	2.81	3.64	2.81	2.74	3.72	2.75	2.73	5.66	7.44
K_2O	11.89	11.92	10.78	10.38	12.06	12.05	12.20	10.85	11.96	11.94	10.85	12.30	12.21	7.25	4.05
Total	*101.57*	*101.40*	*101.56*	*101.23*	*101.19*	*101.54*	*101.79*	*101.55*	*101.73*	*101.73*	*102.25*	*101.73*	*101.56*	*101.69*	*101.91*
Si	2.917	2.929	2.924	2.918	2.926	2.929	2.925	2.937	2.917	2.918	2.930	2.927	2.922	2.935	2.895
Al	1.099	1.081	1.088	1.100	1.088	1.080	1.087	1.079	1.097	1.097	1.081	1.091	1.089	1.082	1.120
Fe	0.004	0.005	0.005	0.004	0.004	0.005	0.010	0.003	0.002	0.005	0.005	0.004	0.004	0.006	0.007
Mg	0.000	0.000	0.000	0.000	0.000	0.000	0.000	0.000	0.000	0.000	0.000	0.000	0.001	0.002	0.000
Ba	0.038	0.038	0.024	0.023	0.034	0.036	0.027	0.022	0.039	0.038	0.031	0.023	0.033	0.003	0.003
Ca	0.007	0.007	0.009	0.011	0.007	0.008	0.007	0.011	0.008	0.009	0.010	0.007	0.009	0.049	0.092
Na	0.245	0.245	0.345	0.353	0.237	0.244	0.247	0.318	0.248	0.241	0.324	0.241	0.241	0.484	0.630
K	0.691	0.694	0.621	0.599	0.702	0.701	0.706	0.623	0.694	0.693	0.622	0.710	0.709	0.408	0.226
Cat sum	*5.002*	*5.000*	*5.015*	*5.008*	*4.999*	*5.003*	*5.008*	*4.994*	*5.005*	*5.001*	*5.003*	*5.003*	*5.009*	*4.970*	*4.973*
Or %	73.28	73.32	63.70	62.21	74.14	73.55	73.57	65.41	73.08	73.45	65.09	74.12	73.93	43.30	23.79
Ab %	26.01	25.92	35.34	36.69	25.07	25.64	25.71	33.40	26.07	25.58	33.91	25.14	25.14	51.44	66.46
An %	0.72	0.76	0.96	1.10	0.78	0.80	0.72	1.18	0.85	0.97	0.99	0.74	0.94	5.26	9.75

riparian forests and coastal swamps is indicated by azonal vegetation (e.g. *Salix*). The preserved root trace fossils in the underlying sandy mudstones, as well as the high content of leaves within the tuff, confirms that the area was overgrown by land plants before the tuff deposition.

The presence of elliptical ash accretionary pellets indicated syn-depositional deformation from a wet landing or gliding. Consequently, post-depositional deformation under the load of the overlying sediments is out of question. Wet landing is typical for fall deposits in terrestrial environment (e.g., Brown et al. 2010, 2012; Eaton & Wilson 2013). This is consistent with the original interpretation of the Kuchyňa tuff as an ash-fall deposit (Šimon et al. 2009) and with the assumed terrestrial environment of the Devínska Nová Ves Fm. (Fordinál et al. 2010, 2012a; Polák et al. 2012). However, deformation of ash pellets (Fig. 3d) can be also linked with gliding of the tuff in a plastic state. Sliding of wet, freshly deposited tuff is supported by various deformations of fossil leaves inside the ash layers. Some movement can also be interpreted based on the angular discontinuity between the underlying muddy sandstones and the tuffs (Fig. 2). The overall tilt of the layers may be caused by a nearby normal fault that was active before deposition of the tuff.

The admixture of nonvolcanic, rounded granule to pebble size clasts in the upper part of the tuff indicate rainwash conditions, which caused some reworking at the end of the process. Since the ~30 cm thick upper part is reworked (epiclastic) the total thickness needs to be reduced to ~70 cm. The non-volcanic admixture is only partially compatible with Devínska Nová Ves Fm. conglomerates (Vass et al. 1988; Fordinál et al. 2010) and documents surface exposure of the biotite paragneisses in the vicinity.

Origin of the tuff

Due to the poor outcropping conditions and high level of fracturing of the section it is very difficult to interpret the original bedding features. The presence of an original bedding plane is supported by leaf accumulation at the base of some beds. The fact that the tuff does not contain any interlayer of non-volcanic material points to a deposit which originated from a single eruption event. Detected grain size variation indicates decrease in intensity of volcanic activity during this time. The clast supported accretionary lapilli bed (n.5, Fig. 2) and graded intervals indicate ash-fall. Large, complexly layered accretionary lapilli or fractured aggregates typical for pyroclastic density flows (e.g., Brown et al. 2010, 2012; Eaton & Wilson 2013) have not been observed. Additionally, the presence of ash pellets (accretionary lapilli) points to wet conditions within the eruption cloud. This can be caused by phreatomagmatic eruptions or by presence of rain moisture. However, phreatomagmatic eruptions, caused by contact of magma and water saturated sediments, typically generate accidental clasts (clast of surrounding sediments; White 1996; Németh & Martin 2007) and in the Kuchyňa tuff, the portion of accidental clasts is very low, and nonvolcanic clasts are metamorphic in origin (gneisses). Therefore, based on the thickness together with the ash-fall origin, and composition (dominance glass shards and one layer of clast supported lapilli tuff), the Kuchyňa tuff was most likely derived from a Plinian type (phreato-Plinian) eruption. In this case, formation of ash pellets was probably caused by presence of rain clouds typical for the determined subtropical humid climate.

A relative proximity to the volcanic centre can also be deduced from grain size of accretionary pellets that are more

Table 5: Composition of mafic minerals and apatite. Chemical composition of amphiboles was calculated after Hawthorne et al. (2012) using the Excel spreadsheet by Locock (2014). Composition of pyroxene was calculated based on 6 oxygens. Content of Fe^{3+} was calculated from stechiometry after Droop (1987). Biotite was normalized to a 22 cation charges after Rieder et al. (1998). Apatite was calculated based on 26 anions.

	amphibole					apatite			biotite				pyroxene			
Analyse	25	26	27	33		6/19	7/19		23	24	30		31	34	32	29
Formula	Prg	Prg	Prg	Mg-Hbl		fluorapatite			Ann	Ann	Ann		En	En	Aug	Aug
SiO_2	43.62	42.84	44.18	44.42	P_2O_5	41.77	40.73	SiO_2	35.86	35.54	36.12	SiO_2	51.19	53.88	52.44	52.11
TiO_2	2.39	2.32	2.68	2.19	SiO_2	0.28	0.27	TiO_2	3.81	4.42	4.35	TiO_2	0.11	0.31	0.51	0.48
Al_2O_3	10.67	10.11	10.57	9.51	UO_2	0.03	0.02	Al_2O_3	13.47	13.75	13.98	Al_2O_3	0.89	1.27	1.70	1.86
Cr_2O_3	0.02	0.02	0.00	0.00	ThO_2	0.04	0.00	Cr_2O_3	0.01	0.00	0.00	Cr_2O_3	0.00	0.01	0.02	0.00
MnO	0.23	0.58	0.19	0.24	Al_2O_3	0.03	0.03	MnO	0.31	0.23	0.18	MnO	0.85	0.50	0.33	0.27
FeO	14.07	18.57	13.39	16.42	La_2O_3	0.07	0.05	FeO	23.30	22.87	22.85	FeO	27.64	18.61	9.98	9.30
MgO	12.68	9.52	13.19	11.29	Ce_2O_3	0.39	0.34	MgO	7.71	8.38	8.25	MgO	17.32	23.84	14.32	14.50
CaO	11.10	10.90	11.45	10.72	Y_2O_3	0.17	0.06	CaO	0.24	0.06	0.07	CaO	1.27	1.51	20.37	20.88
Na_2O	2.01	2.01	1.98	1.84	MnO	0.14	0.22	Na_2O	0.34	0.41	0.41	Na_2O	0.01	0.02	0.27	0.29
K_2O	0.57	0.59	0.59	0.60	FeO	0.55	0.24	K_2O	8.14	8.44	8.36	*Total*	*99.28*	*99.98*	*99.93*	*99.71*
F	0.00	0.00	0.00	0.00	MgO	0.00	0.00	F	0.00	0.00	0.00	Si	1.980	1.975	1.958	1.944
Cl	0.03	0.02	0.02	0.05	CaO	54.19	54.85	Cl	0.24	0.18	0.21	^{T}Al	0.020	0.025	0.042	0.056
Init. Tot.	*97.37*	*97.49*	*98.29*	*97.27*	SrO	0.03	0.04	*Total*	*93.42*	*94.28*	*94.78*	Al	0.020	0.030	0.032	0.026
*FeO	12.14	16.86	11.78	14.53	Na_2O	0.04	0.01	Si	2.853	2.799	2.821	Fe^{3+}			0.001	0.026
*Fe_2O_3	2.14	1.90	1.79	2.10	K_2O	0.00	0.00	^{T}Al	1.147	1.201	1.179	Ti	0.003	0.009	0.014	0.014
*$H2O^{+}$	2.03	1.98	2.04	2.01	F	2.36	2.08	Al	0.116	0.074	0.108	Cr	0.000	0.000	0.001	0.000
Total	*99.62*	*99.66*	*100.51*	*99.49*	Cl	0.48	0.47	Ti	0.228	0.262	0.255	Mg	0.999	1.303	0.797	0.807
Si	6.448	6.482	6.456	6.627	*Total*	*100.5*	*99.41*	Fe	1.550	1.506	1.492	Fe^{2+}	0.894	0.571	0.311	0.264
^{T}Al	1.552	1.518	1.544	1.373	P	5.993	5.806	Mg	0.914	0.984	0.961	Mn	0.028	0.016	0.010	0.008
Ti	0.265	0.264	0.295	0.246	Si	0.047	0.045	Mn	0.021	0.016	0.012	Ca	0.053	0.059	0.815	0.835
^{C}Al	0.307	0.285	0.277	0.300	Th	0.002	0.000	Cr	0.001	0.000	0.000	Na	0.001	0.001	0.019	0.021
Cr	0.002	0.003	0.000	0.000	U	0.001	0.001	Ca	0.020	0.005	0.006	*Cat sum*	*3.997*	*3.989*	*4.000*	*4.001*
Fe^{3+}	0.239	0.216	0.196	0.236	La	0.004	0.003	K	0.826	0.848	0.833					
$^{C}Fe^{2+}$	1.392	2.085	1.352	1.707	Ce	0.024	0.021	Na	0.052	0.063	0.063					
Mg	2.795	2.147	2.873	2.511	Y	0.015	0.006	*Cat sum*	*7.727*	*7.757*	*7.728*					
$^{B}Mn^{2+}$	0.028	0.075	0.024	0.030	Al	0.006	0.005									
$^{B}Fe^{2+}$	0.109	0.049	0.088	0.105	Fe	0.078	0.034									
^{B}Ca	1.758	1.768	1.792	1.713	Mn	0.021	0.032									
^{B}Na	0.105	0.108	0.095	0.152	Mg	0.000	0.000									
^{A}Na	0.471	0.480	0.465	0.382	Ca	9.839	9.896									
K	0.108	0.114	0.110	0.115	Sr	0.003	0.004									
O	22.000	22.000	22.000	22.000	Na	0.013	0.004									
OH	1.992	1.995	1.995	1.988	K	0.000	0.000									
F	0.000	0.000	0.000	0.000	OH	0.593	0.759									
Cl	0.008	0.005	0.005	0.012	F	1.267	1.107									
Cat sum	*15.579*	*15.594*	*15.573*	*15.497*	Cl	0.139	0.134									

than 5 mm in diameter. This usually indicates deposition in a radius of 10s of km from the source (Brown et al. 2012). Only in the case of extremely large eruptions can the pellets be deposited at a distance larger than 100 km.

The characterization of the parental magma is difficult, because the Kuchyňa tuff contains high proportions of slightly altered volcanic glass and its actual composition is also influenced by segregation during transportation and deposition. The monocrystalline quartz, plagioclase, sanidine, non-altered biotite, amphibole and vitroclasts of the first type (microlithe free) can be considered juvenile. The crystalloclasts of Px and basic plagioclase (An_{79}) together with microlithic glass can be sourced from the magma chamber or may have been incorporated during explosions, from older volcanic rocks. Based on the results of chemical analyses, presence of sanidine crystalloclasts and based on plagioclase composition ($An_{37–52}$), the Kuchyňa tuff can be diagnosed as high-K calk–alkaline rhyodacite (Fig. 5). Higher LREE content, depletion in P, Nb, Ta, Ti and enrichment in Pb (Fig. 5e, f) is typical for subduction related magmas (Bailey 1981). The K_2O–Rb ratio as well as the values of Rb, Ba, Pb, La, Zr, Hf, K/La, La/Y, Zr/Y, Hf/Yb, Ni/Co, Sc/Ni (Table 2) show affinity to the Andean arc type volcanism (thick continental margins; Bailey 1981). These signatures are typical for the Western Segment of the Carpathian–Pannonian region (e.g., Konečný et al. 1995, 1998, 2002; Karátson et al. 2000, 2007; Seghedi et al. 2004), where volcanic activity in the Badenian is linked with subduction related back-arc extension, for example, with the syn-rift stage of the Pannonian Basin system (e.g., Seghedi et al. 2004; Kováč et al. 2007). In this case, subduction-induced, mantle-derived magmas were affected by long-term fluid and sediment contamination as well as by mixing of crustal melts with mantle-derived magmas (Seghedi et al. 2004; Harangi & Lenkey 2007). Based on these facts, the origin of the Kuchyňa tuff must be somewhere within the Western segment of the Pannonian Basin System.

If the source area really is in the Western segment of the Pannonian Basins, the Kuchyňa tuff must have been transport from the East towards the West. This is in accordance with findings of Lukács et al. (2018) from the Bükkalja Volcanic Field. Moreover, similar interpretations about the Pannonian source (based on the $^{143}Nd/^{144}Nd$ ratio) which indicates East to West transport of silicic tuffs (16.1–14.5 Ma), comes from the Upper Freshwater Molasse in Germany (Rocholl et al. 2008; Aziz et al. 2010).

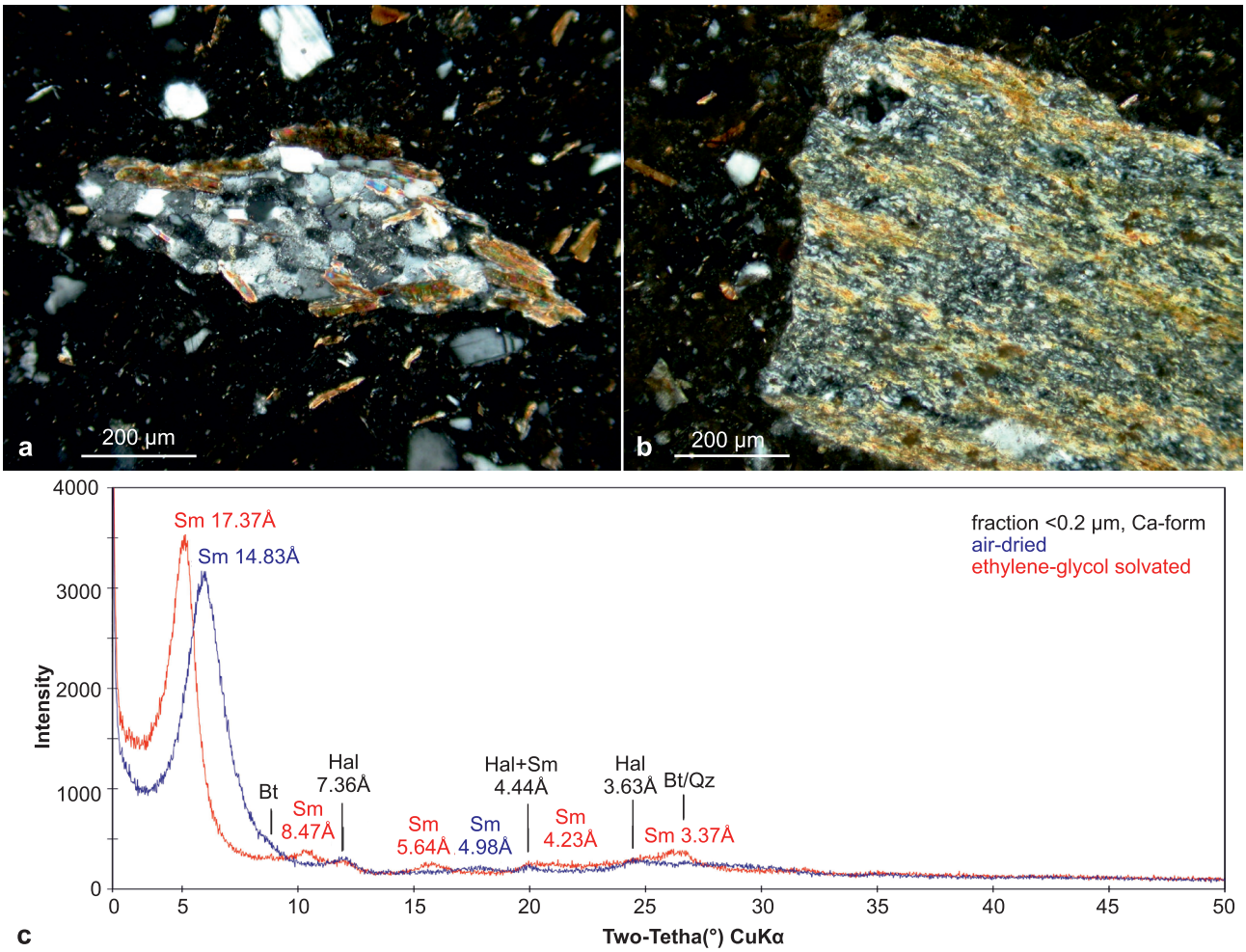

Fig. 7. a — Bt-paragneiss lithoclast in tuff, crossed polars; **b** — Qz-mica shale lithoclast in tuff, crossed polars; **c** — clay fraction X-ray record from an oriented slide. Sm — smectite, Hal — halloysite, Bt — biotite, Qz — quartz.

Source of the Kuchyňa Tuff

In general, the Badenian or younger silicic volcanism was focused further south in the Pannonian Basin (e.g., Pécskay et al. 2006; Lexa et al. 2010). The comparison of the different ages of the volcanic activity is often complicated due to the variation in quality of the dating methods. However, some radiometric ages have been refined in the recent years by U/Pb and Ar/Ar dating (e.g., Lukács et al. 2018).

The deposition of the Kuchyňa tuff is relatively synchronous with a large caldera-forming eruption in the Bükkalja Volcanic Field (Lukács et al. 2018). This volcanic event produced high amounts of ignimbrites and tuffs, which were marked as the Demjén Unit. The Demjén Unit forms a key stratigraphic horizon in the Pannonian Basin with an age of 14.88±0.014 Ma (Lukács et al. 2018). This unit is formed by a high-K dacite–rhyodacite ignimbrite, ash flow and fall deposits composed of plagioclase, biotite, amphibole, ±quartz. This is relatively consistent with the composition of the Kuchyňa tuff. However, the Demjén Unit has a well characterized trace element pattern with depleted heavy rare earth elements and no pronounced negative Eu-anomaly (Eu/Eu*= 0.8–0.9; Lukács et al. 2018; Fig. 5). The Kuchyňa tuff, on the other hand, displays an Eu-anomaly of 0.59 (Table 2, which questions their connection. Another significant horizon is the Dej tuff (Transylvanian Basin), which was dated to

Table 6: CIPW normative calculation of the Kuchyňa tuffs. All Fe was calculated as FeO.

	wt. % normative minerals			
Layer	n-1	n-3	n-4	n-5
quartz	32.27	35.06	37.11	35.82
corundum	10.37	9.90	6.14	7.51
orthoclase	10.52	14.71	20.09	20.27
albite	11.42	10.58	11.34	13.45
anorthite	9.83	6.41	6.88	4.60
diopside	0.00	0.00	0.00	0.00
hypersthene	10.49	8.84	8.19	7.49
magnetite	0.00	0.00	0.00	0.00
hematite	0.00	0.00	0.00	0.00
ilmenite	0.00	0.00	0.00	0.00
apatite	0.14	0.07	0.07	0.14
rutile	0.25	0.15	0.12	0.23
calcite	0.50	0.07	0.17	1.42

14.8–15.1 Ma (K/Ar, Ar/$A_{multigrain}$, FT; Szakács et al. 2012). The tuff is subduction related and similar in composition: quartz, plagioclase, biotite, K-feldspar, amphibole±pyroxene. But, de Leeuw et al. (2013) updated this age to 14.38 Ma based on single grain Ar/Ar dating, and this age is not compatible with the Kuchyňa tuff.

On the other hand, the source area of the Kuchyňa tuff may be found in the nearby Börzsöny–Pilis–Visegrád volcanic field or in the Central Slovakian volcanic field (after Lexa et al. 2010). In the time of Kuchyňa tuff deposition, the Börzsöny–Pilis–Visegrád sub-region was much closer to the juvenile Danube and Vienna basins and also to the Carpathian Foredeep (e.g., Kováč 2000; Kováč et al. 2017; Fig. 9). In this region dacitic and andesitic volcanism with a similar age range is present and three small-scale caldera forming events were described (Karátson et al. 2000, 2007; Fig. 5). But around 15 Ma, andesitic activity dominated, which again questions the connection with Kuchyňa tuff. However, this area remains one of the best candidates for the source of the Kuchyňa tuff.

Activity of the Central Slovak volcanic field starts in shallow water condition (Vinica, Nerestnica fms.). These deposits of a freatomagmatic eruption were previously dated to ~16.4–15.9 Ma (Konečný in Konečný et al. 1988) but were recently redated to 15 Ma (Chernyshev et al. 2013). However, these volcanic and volcanoclastic rocks (tuffs) are mainly amphibole andesite in composition (amphibole, plagioclase, ±pyroxene, garnet, quartz, biotite), which excludes connection with the Kuchyňa tuff (Fig. 5). Some rhyodacite tuffs occur below the Vinica formation, but these ranked to the early Miocene (Konečný et al. 1998). In this region, volcanic activity continues with formation of andesitic volcanos and stratovolcanoes (Konečný et al. 1995; Lexa et al. 2010). Rhyolitic volcanism in the Central Slovak volcanic field (Jastrabá and Strelníky fms.), as well as rhyolitic volcanism in the southern part of East Slovakia can be excluded due to their mostly Sarmatian (late Serravallian) age 13–11 Ma (e.g., Pécskay et al. 2002, 2006; Demko 2010; Chernyshev et al. 2013). So, these volcanic fields cannot be connected to the Kuchyňa tuff.

Another potential source is in the neighbouring Danube basin, where buried Badenian volcanic centres are present (Šurany, Kráľová, Rusovce, Trakovice centers; e.g., Hrušecký 1999; Vass 2002; Kronome et al. 2014; Rybár et al. 2016). But they are also formed by products of biotite-amphibole to pyroxene andesite volcanism (Kantor 1987; Mihálíková 1962; Gaža 1966; Rybár et al. 2016). However, information about composition of these volcanoes comes only from discontinuous well cores, still sourcing from these centres is unlikely, but cannot be fully excluded. Additionally, in the Slovak part

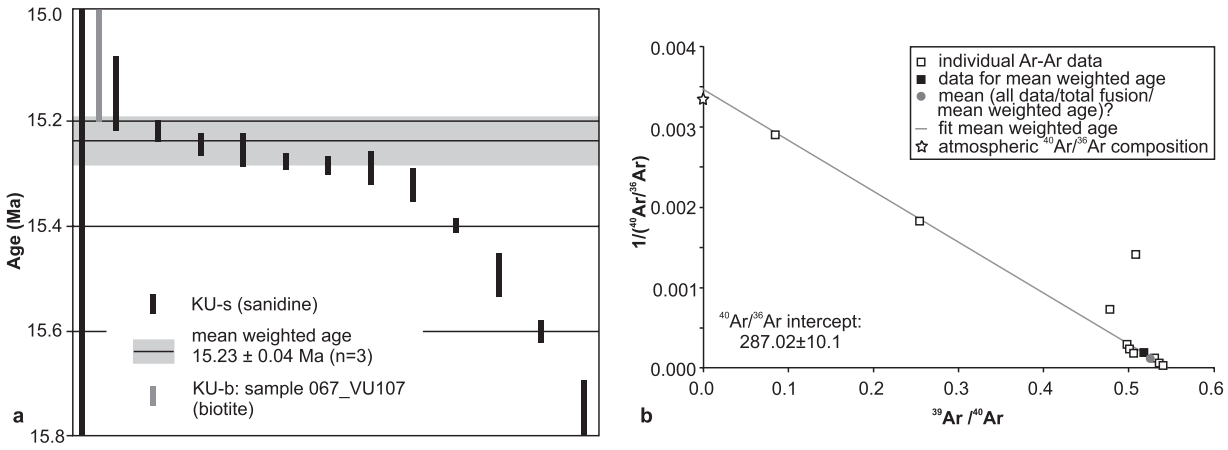

Fig. 8. a — Summary of the single grain $^{40}Ar/^{39}Ar$ data with error bars for different groups of grains and the mean weighted age of KU (Kuchyňa tuff) sample (see legend). **b** — Inverse isochron; the grey line is defined by the grains included for the mean weighted age calculation. The star represents the atmospheric $^{40}Ar/^{36}Ar$ composition. All errors are given at 2σ.

Table 7: Fission track analyses with their calculated ages (MAKUCH01-sample). First row (AP) does not contain grains with low density tracks. Abbreviations are as follows: AP=apatite; ZR=zircon; N_{grains} is the total number of grains counted; N_{rej} represent the number of grains rejected from final age calculation respectively; ρs and ρi (tracks/cm^2) are spontaneous and induced track densities respectively; Ns and Ni are the number of spontaneous and induced tracks counted respectively; P(χ2) is the probability obtaining Chi-square (χ^2) for n degrees of freedom (where n is the number of crystals minus 1); age represents a central age for samples that pass P(χ^2) at 5%, otherwise the mean age is reported (in bold italics); the age is reported with the 1σ standard error (±1σ); D is dispersion in single grain age (Galbraith and Laslett 1993); U is U-content in parts per million; Dpar is average etch pit diameter given with 1σ standard deviation (SD Dpar).

			Age data											Length data			
Mineral	N_{grains}	N_{rej}	ρ_s	N_s	ρ_i	N_i	**P(χ^2)**	**Age**	**±1σ**	**D**	**U**	D_{par}	SD_{Dpar}	**MTL**	**±1σ**	SD_L	N_L
			×10^6 cm^{-2}		**×10^6 cm^{-2}**		**%**	**Ma**	**Ma**	**ppm**	**µm**		**µm**				
AP	24	0	0.008	35	0.121	547	100.00	14.5	2.8	0.00	116	1.6	0.6	–	–	–	–
AP	31	0	0.007	35	0.126	656	99.96	12.1	2.3	0.00	119	1.6	0.6	–	–	–	–
ZR	15	0	0.45	498	0.735	814	93.87	13.7	1.2	0.00	7121	-	-	-	-	-	-

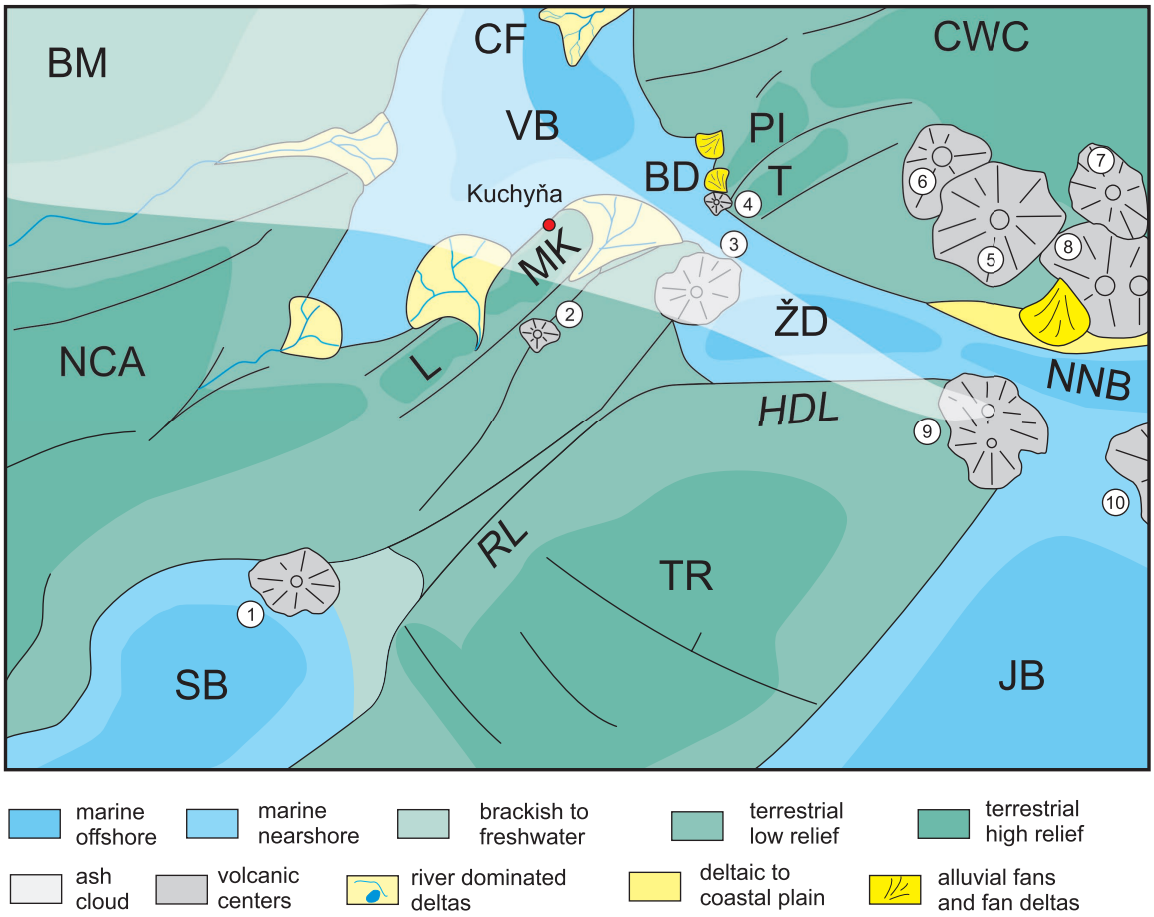

Fig. 9. Paleogeographic reconstruction of the North-Western part of the Carpathian–Pannonian Region showing the possible transport direction of the ash cloud, which deposited the Kuchyňa tuff. BM — Bohemian massif; NCA — Northern Calcareous Alps; L — Leitha Mts.; MK — Malé Karpaty Mts.; PI — Považský Inovec Mts.; T — Tribeč Mts.; CWC — Central Western Carpathians; TR — Transdanubian Range; CF — Carpathian Foredeep; SB — Styrian Basin; VB — Vienna Basin; BD — Blatné Depression (Danube Basin); ŽD — Želiezovce Depression (Danube Basin); NNB — Novohrad Nógrád Basin; JB — Jászág Basin; *RL* — Rába Line, *HDL* — Hurbanovo–Diósjenő Line. Volcanic centers: 1 — Styrian Basin, 2 — Rusovce, 3 — Kráľová, 4 — Trakovice, 5 — Štiavnica stratovolcano, 6 — Vtáčnik, 7 — Javorie, 8 — Čelovce, 9 — Visegrád-Börzsöny-Burda, 10 — Mátra. The image was modified after Kováč (2000); Pécskay et al. (2006) and Kováč et al. (2017, 2018).

of the Danube Basin, tuff layers occur within the calcareous nannofossil NN5 Zone (14.9–13.5 Ma; Martini 1971), for example, in the Trakovice-4, Cífer-2, Špančince-4, Modrany-2 wells (Rybár et al. 2016; Csibri et al. 2018; Hudáčková et al. 2018). Furthermore, all these Danube Basin tuffs show different trace element associations (Fig. 5), thus they cannot be associated with the Kuchyňa tuff.

Finally, the tuffs in the Western Carpathian Foredeep need to be also considered. Two main phases of felsic tuffs were dated by zircon FT; lower Miocene 20.3±2.4 Ma and middle Miocene 16.2±2.1 Ma (Nehyba 1997; Nehyba et al. 1999; Nehyba & Roetzel 1999). However, the results of the presented study show that the FT data may be incoherent. Additionally, the lower Miocene tuffs from the south-eastern margin of the Bohemia Massif were refined by $^{40}Ar/^{39}Ar$ to 17.23 Ma (Roetzel et al. 2014) and the middle Miocene tuffs located on the Czech–Polish boundary (North-Western Carpathian Foredeep Basin) were dated by $^{40}Ar/^{39}Ar$ to 14.27±0.03 Ma (Bukowski et al. 2018). So again connection to the Kuchyňa tuff cannot be confirmed.

In summary, the Kuchyňa tuff cannot be clearly connected to a particular volcanic centre. However, the Börzsöny–Pilis–Visegrád sub-region and the Demjén unit are the best potential candidates for the source of the Kuchyňa tuff. With regard to other tuff occurrences, the Kuchyňa tuff can only be clearly correlated with the above mentioned tuffite from the Bernhardsthal-4 well, Vienna Basin (Sant et al. in press).

Conclusions

The deposition of the Kuchyňa tuff took place in terrestrial conditions, short before the onset of the Badenian (Langhian) transgression of the Central Paratethys Sea. Fossil leaves indicate subtropical climate with evergreen broadleaved forests. The studied rhyodacitic, fine grained and lapilly tuffs were

produced by an explosive, possibly Plinian eruption. The Ar/Ar single grain sanidine age of 15.23±0.04 Ma is interpreted as the age of this eruption. The origin of the Kuchyňa tuff can be connected with the syn-rift stage of the Pannonian Basin system and the tuff most likely originated in the northern parts of the basin (Börzsöny–Pilis–Visegrád sub-region) and was transported towards the West.

Acknowledgements: This research was supported by the Slovak Research and Development Agency under contracts No. APVV-16-0121, APVV-15-0575, APVV-0315-12; by the Netherlands Geosciences Foundation (ALW) with funding from the Netherlands Organization for Scientific Research (NWO) by VICI grant 865.10.011 of WK; by Grants UK/70/2019 and UK/211/2019. The authors wish to express their gratitude to T. Csibri, M. Jamrich, T. Klučiar, A. Lačný, M. Šujan from Comenius University in Bratislava for help during field work and sampling. A special thanks goes to Roel van Elsas for his support in the mineral separation lab at the VU University and to A. Biroň from the Earth Science Institute of the SAS for X-ray diffraction analysis. We also express gratitude the Editors and Reviewers for guidance and insightful comments.

References

Ash A., Ellis B., Hickey L.J., Johnson K., Wilf P. & Wing S. 1999: Manual of Leaf Architecture — morphological description and categorization of dicotyledonous and net-veined monocotyledonous angiosperms by Leaf Architecture Working Group. *Smithsonian Institution*, Washington, 1–65.

Aziz H.A., Böhme M., Rocholl A., Prieto J., Wijbrans J.R., Bachtadse V. & Ulbig A. 2010: Integrated stratigraphy and $^{40}Ar/^{39}Ar$ chronology of the early to middle Miocene Upper Freshwater Molasse in western Bavaria (Germany). *Int. J. Earth. Sci. (Geol. Rundsch.)* 99, 1859–1886.

Bailey J.C. 1981: Geochemical criteria for a refined tectonic discrimination of orogenic andesites. *Chem. Geol.* 32, 139–154.

Barrett T.J. & MacLean W.H. 1994: Chemostratigraphy and hydrothermal alteration in exploration for VHMS deposits in greenstones and younger volcanic rocks. In: Lentz D.R. (Eds.): Alteration and alteration processes associated with ore-forming systems. *Geological Association of Canada, Short Course Notes* 11, 433–467.

Bondarenková Z., Zbořil Ľ. & Motlíková H. 1980: Bratislava–Rusovce-geothermal well HGB-1, exploration HGP, aim: possibilities of goethermal reservoirs in this area. *Open file report*, *Geofond*, Bratislava, No. 48993 (in Slovak).

Brown R.J., Branney M.J., Maher C. & Dávila-Harris P. 2010: Origin of accretionary lapilli within ground-hugging density currents: Evidence from pyroclastic couplets on Tenerife. *GSA Bulletin* 122, 1–2, 305–320.

Brown R.J., Bonadonna C. & Durant A.J. 2012: A review of volcanic ash aggregation. *Phys. Chem. Earth* 45–46, 65–78.

Bukowski K., Sant K., Pilarz M., Kuiper K. & Garecka M. 2018: Radio-isotopic age and biostratigraphic position of a lower Badenian tuffite from the western Polish Carpathian Foredeep Basin (Cieszyn area). *Geol. Quarterly* 62, 2, 303–318.

Carlson W.D., Donelick R.A. & Ketcham R.A. 1999: Variability of apatite fission-track annealing kinetics: I. Experimental results. *Am. Mineral.* 84, 9, 1213–1223.

Chernyshev I.V., Konečný V., Lexa J., Kovalenker V.A., Jeleň S., Lebedev V.A. & Goltsman Y.V. 2013: K–Ar and Rb–Sr geochronology and evolution of the Štiavnica Stratovolcano (Central Slovakia). *Geol. Carpath.* 64, 4, 327–351.

Csibri T., Rybár T., Šarinová K., Jamrich M., Šarinová K., Sliva Ľ. & Kováč M. 2018: Miocene fan delta conglomerates in the north-western part of the Danube Basin: provenance, paleoenvironment, paleotransport and depositional mechanisms. *Geol. Carpath.* 69, 5, 467–482.

de Leeuw A., Filipescu S., Maţenco L., Krijgsman W., Kuiper K. & Stoica M. 2013: Paleomagnetic and chronostratigraphic constraints on the Middle to Late Miocene evolution of the Transylvanian Basin (Romania): Implications for Central Paratethys stratigraphy and emplacement of the Tisza–Dacia plate. *Global Planet. Change* 103, 82–98.

Demko R., Lexa J., Koděra P., Biroň A., Smolka J., Šesták P., Konečný P., Tuček Ľ., Ferenc Š., Bačo P., Repčiak M., Kollárová V., Pipík Kiška R., Mikušová J., Kotulová J., Bystrická G. & Vlachovič J. 2010: Paleovolcanic reconstruction maps of rhyolite volcanics of Slovakia an analysis of magmatic and hydrotermal processes. Final report of the geological task 15 06. *Open file report*, *Geofond*, Bratislava, 1–728 (in Slovak).

Droop G.T.R. 1987: A general evaluation for estimating Fe^{3+} concentrations in ferromagnesian silicates and oxides from microprobe analyses, using stoichiometric criteria. *Mineral. Mag.* 51, 431–435.

Dunkl I. 2002: Trackkey: a Windows program for calculation and graphical presentation of fission track data. *In Computers and Geosciences* 28, 1, 3–12.

Eaton A.R. & Wilson C.J.N. 2013: The nature, origins and distribution of ash aggregates in a large-scale wet eruption deposit: Oruanui, New Zealand. *Journal of Volcanology and Geothermal Research* 250, 129–154.

Ellis B., Daly D.C., Hickey L.J., Johnson K., Mitchell J.D., Wilf P. & Wing S. 2009: Manual of Leaf Architecture. *Cornell University Press*, Cambridge, USA, 1–190.

Fleischer R.L. & Price P.B. 1964: Techniques for geological dating of minerals by chemical etching of fission fragment tracks. *Geochim. Cosmochim. Acta* 28, 10–11, 1705–1714.

Fordinál K., Baráth I., Šimon L., Kohút M., Nagy A. & Kučerová J. 2010: New data on the Devínska Nová Ves Formation (Vienna Basin, Slovakia). 16th Conference on Upper Tertiary Brno. *Geol. Výzk. Mor. Slez.,* Brno, 32–34 (in Slovak with English abstract).

Fordinál K., Maglay J., Elečko M., Nagy A., Moravcová M., Vlačiky M., Kohút M., Németh Z., Bezák V., Polák M., Plašienka D., Olšavský M., Buček S., Havrila M., Hók, J., Pešková I., Kucharič L., Kubeš P., Malík P., Baláž P., Liščák P., Madarás J., Šefčík P., Baráth I., Boorová D., Uher P., Zlínska A. & Žecová K. 2012a: Explantions for the geological map of the Vienna Basin, 1:50 000. *State Geological institute of Dionýz Štúr*, 1–232 (in Slovak).

Fordinál K., Maglay J., Elečko M., Nagy A., Moravcová M., Vlačiky M., Kučera M., Polák M., Plašienka D., Filo I., Olšavský M., Buček S., Havrila M., Kohút M., Bezák V. & Németh Z. 2012b: Geological map of the Záhorská nížina lowland, 1:50 000. *State Geological institute of Dionýz Štúr*.

Gallagher K., Brown R. & Johnson C. 1998: Fission track analysis and its application to geological problems. *Annual Review of Earth and Planetary Sciences* 26, 1, 519–572.

Galbraith R.F. 1981: On statistical models for fission track counts. *Mathematical Geology* 13, 6, 471–478.

Galbraith R.F. & Laslett G.M. 1993: Statistical models for mixed fission track ages. *Nuclear Tracks and Radiation Measurements* 21, 4, 459–470.

Gaža B. 1966: Geological evaluation of the Kráľová-1 well. *Open file report*, *Geofond*, Bratislava, No. 16971 (in Slovak).

Gleadow A.J.W. & Duddy I.R. 1981: A natural long-term track annealing experiment for apatite. *Nuclear Tracks* 5, 1–2, 169–174.

Green P.F. & Duddy I.R. 1989: Some comments on palaeotemperature estimation from apatite fission track analysis. *J. Petrol. Geol.* 12, 111–114.

Green P.F., Duddy I.R., Gleadow A.J.W., Tingate P.R. & Laslett G.M. 1986: Thermal annealing of fission tracks in apatite: 1. A qualitative description. *Chemical Geology: Isotope Geoscience section* 59, 237–253.

Harangi Sz. & Lenkey L. 2007: Genesis of the Neogene to Quaternary volcanism in the Carpathian-Pannonian region: Role of subduction, extension, and mantle plume. In: Beccaluva L., Bianchini G. & Wilson M. (Eds.): Cenozoic Volcanism in the Mediterranean Area. *Geological Society of America, Special Paper* 418, 67–92.

Harangi Sz., Vaselli O., Tonarini S., Szabó Cs., Harangi R. & Coradossi N. 1995: Petrogenesis of Neogene extension-related alkaline volcanic rocks of the Little Hungarian Plain Volcanic Field (Wester Hungary). *Acta Vulcanol.* 7, 2, 173–187.

Hastie A.R., Kerr A.C., Pearce J.A. & Mitchell S.F. 2007: Classification of Altered Volcanic Island Arc Rocks using Immobile Trace Elements: Development of the Th-Co Discrimination Diagram. *J. Petrol.* 48, 12, 2341–2357.

Hawthorne F.C., Oberti R., Harlow G.E., Maresch W.V., Martin R.F., Schumacher J.C. & Welch M.D. 2012: IMA report, nomenclature of the amphibole supergroup. *Am. Mineral.* 97, 2031–2048.

Hrušecký I. 1999: Central part of the Danube Basin in Slovakia: Geophysical and geological model in regard to hydrocarbon prospection. *Exploration Geophysics, Remote Sensing and Environment Journal* 6, 1, 1–65.

Hudáčková N., Kováč M., Ruman A., Halásová E., Jamrich M., Kováčová M., Rybár S., Šujan M., Šarinová K: 2018: Biostratigraphy and paleoenvironmental interpretation of the Špačince-4 & Dubové-2 wells sedimentary record. *Open file report*, archive Nafta l.t.d.

Hurford A.J. & Green P.F. 1983: The zeta age calibration of fission-track dating. *Chem. Geol.* 41, 285–317.

Jackson M.L. 1975: Soil Chemical Analysis — Advanced Course. *M.L. Jackson*, Madison, 1–895.

Kantor J. 1987: Isotop study and radiometric dating in the vicinity of greate Bratislava. *Open file report*, *Geofond*, Bratislava, No. 65227 (in Slovak).

Karátson D., Márton E., Harangi S., Józsa S., Balogh K., Pécskay Z., Kovácsvölgyi S., Szakmány G. & Dulai A. 2000: Volcanic evolution and stratigraphy of the Miocene Börzsöny Mountains, Hungary: An integrated Study. *Geol. Carpath.* 51, 5, 235–343.

Karátson D., Oláh I., Pécskay Z., Márton E., Harangi S., Dulai A., Zelenka T. & Kósik S. 2007: Miocene volcanism in the Visegrád Mountains (Hungary): an integrated approach to regional volcanic stratigraphy. *Geol. Carpath.* 58, 6, 541–563.

Konečný P. & Lexa J. 2002: Evolution of the Central Slovakia neogene volcanic field related to the horst/graben structure. *Geol. Carpath.* 53, special issue, Proceedings of XVII. Congress of Carpathian-Balkan Geological Association, Bratislava, Sept. 1–4, http://www.geologicacarpathica.com/special-issues/53-2002/.

Konečný P., Lexa J. & Konečný V. 2002a: Evolution of the Banská Štiavnica Stratovolcano and corresponding magma chamber (Central Slovakia). *Geol. Carpath.* 53, special issue, Proceedings of XVII. Congress of Carpathian-Balkan Geological Association, Bratislava, Sept. 1–4, http://www.geologicacarpathica.com/special-issues/53-2002/.

Konečný V., Lexa J. & Hojstovičová V. 1995: The Central Slovakia Neogene volcanic field: a review. *Acta Vulcanol.* 7, 2, 63–78.

Konečný V., Lexa J., Halouzka R., Hók J., Vozár J., Dublan L., Nagy A., Šimon L., Havrila M., Ivanička J., Hojstovičová V., Miháliková A., Vozárová A., Konečný P., Kováčikova M., Filo M., Marcin D., Klukanová A., Liščák P. & Žáková E. 1998: Explanations to the geological map of Štiavnica Mts. and Pohronský Inovec Mts. (Štiavnica stratovolcano). *State Geological institute of Dionýz Štúr*, Bratislava, 1–473 (in Slovak with English summary).

Konečný V., Kováč M., Lexa J. & Šefara J. 2002b: Neogene evolution of the Carpatho–Pannonian region: an interplay of subduction and back-arc diapiric uprise in the mantle. *EGU Stephan Mueller Special Publication Series* 1, 105–123.

Koppers A.A.P. 2002: ArArCALC F software for $^{40}Ar/^{39}Ar$ age calculations. *Computers and Geosciences* 28, 605–619.

Kováč M. 2000: Geodynamic, Paleogeographic and structural development of the Carpatho–Pannonian region during the Miocene: New view on the Neogene basins of Slovakia. *Veda*, Bratislava, 1–202 (in Slovak).

Kováč M., Andreyeva-Grigorovitch A., Bajraktarević Z., Brzobohatý R., Filipescu S., Fodor L., Harzhauser M., Nagymarosy A., Oszcypko N., Pavelić D., Rögl F., Saftić B., Sliva Ľ. & Studencka B. 2007: Badenian evolution of the Central Paratethys Sea: paleogeography, climate and eustatic sea-level changes. *Geol. Carpath.* 58, 6, 579–606.

Kováč M., Hudáčková, N., Halásová E., Kováčová M., Holcová K., Oszczypko-Clowes M., Báldi K., Less G., Nagymarosy A., Ruman A., Klučiar T. & Jamrich M. 2017: The Central Paratethys palaeoceanography: a water circulation model based on microfossil proxies, climate, and changes of depositional environment. *Acta Geologica Slovaca* 9, 2, 75–114.

Kováč M., Halásová E., Hudáčková N., Holcová K., Hyžn, M., Jamrich M. & Ruman A. 2018: Towards better correlation of the Central Paratethys regional time scale with the standard geological time scale of the Miocene Epoch. *Geol. Carpath.* 69, 3, 283–300.

Kovar-Eder J. & Hably L. 2006: The flora of Mataschen — A unique plant assemblage from the Late Miocene of eastern Styria (Austria). *Acta Palaeobotanica* 46, 2, 157–233.

Kronome B., Baráth I., Nagy A., Uhrin A., Maros G., Berka R. & Černák R. 2014: Geological Model of the Danube Basin; Transboundary Correlation of Geological and Geophysical Data. *Slovak Geological Magazine* 14, 2, 17–35.

Kuiper K.F., Deino A., Hilgen F.J., Krijgsman W., Renne P.R. & Wijbrans J.R. 2008: Synchronizing rock clocks of Earth history. *Science* 320, 500–504.

Le Bas M.J., Le Maitre R.W., Streckeisen A. & Zanettin B. 1986: A Chemical Classification of Volcanic Rocks Based on the Total Alkali-Silica Diagram. *J. Petrol.* 27, 3, 745–750.

Lee J.Y., Marti K., Severinghaus J.P., Kawamura K., Yoo H.S., Lee J.B. & Kim J.S. 2006: A redetermination of the isotopic abundances of atmospheric Ar. *Geochim. Cosmochim. Acta* 70, 4507–4512.

Lexa J., Seghedi I., Németh K., Szakács A., Konečný V., Pécskay Z., Fülöp A. & Kovacs M. 2010: Neogene–Quaternary Volcanic forms in the Carpathian–Pannonian Region: a review. *Central Eur. J. Geosci*. 2, 3, 207–270.

Locock A.J. 2014: An Excel spreadsheet to classify chemical analyses of amphiboles following the IMA 2012 recommendations. *Computers and Geosciences* 62, 1–11.

Lukács R., Harangi S., Guillong M., Bachmann O., Fodor L., Buret Y., Dunkl I., Sliwinski J., von Quadt A., Peytcheva I. & Zimmerer M. 2018: Early to Mid-Miocene syn-extensional massive silicic volcanism in the Pannonian Basin (East-Central Europe): Eruption chronology, correlation potential and geodynamic implications. *Earth-Sci. Rev.* 179, 1–19.

Martini E. 1971: Standard Tertiary and Quaternary calcareous nannoplankton zonation. In: Farinacci A. (Ed.): Proceedings of second Planktonic Conference, Roma. Vol. 2, 739–765.

McDonough W.F. & Sun S.-s. 1995: The composition of the Earth. *Chem. Geol.* 120, 223–253.

McDougall I. & Harrison T.M. 1999: Geochronology and Thermochronology by the $^{40}Ar/^{39}Ar$ Method. 2nd ed. *Oxford University Press*, New York, 1–288.

Miall A.D. 2006: The geology of fluvial deposits. *Springer*, New York, 1–582.

Miháliková A. 1962: Petrographic characteristics of volcanic series of the Š-1 well Šurany. *Open file report*, *Geofond*, Bratislava, No. 12991 (in Slovak).

Min K., Mundil R., Renne P.R. & Ludwig K.R. 2000: A test for systematic errors in $^{40}Ar/^{39}Ar$ geochronology through comparison with U/Pb analysis of a 1.1-Ga rhyolite. *Geochim. Cosmochim. Acta* 64, 73–98.

Nehyba S. 1997: Miocene volcaniclastics of the Carpathian Foredeep in the Czech Republic. *Věstník Českého geologického ústavu* 72, 4, 311–327.

Nehyba S. & Roetzel R. 1999: Lower Miocene Volcaniclastics in South Moravia and Lower Austria. *Jahrbuch der Geologischen Bundesanstalt*, 473–490.

Nehyba S., Roetzel R. & Adamová M. 1999: Tephostratigraphy of Neogene volcaniclastics (Moravia, lower Austria, Poland). *Geol. Carpath.* special issue 50, Proceedings of the International Conference Carpathian Geology 2000, Smolenice, Slovakia, October 11–14, 126–127.

Németh K. & Martin U. 2007: Practical Volcanology, Lecture Notes for Understanding Volcanic Rocks from Field Based Studies. *Geological Institue of Hungary*, Budapest, 1–221.

Pearce J.A. 1996: A User`s Guide to Basalt Discrimination Diagrams. In: Wyman D.A. (Ed.): Trace Element Geochemistry of Volcanic Rocks: Applications for Massive Sulphide Exploration. *Geological Association of Canada*, *Short Course Notes* 12, 79–113.

Pécskay Z., Kaličiak M., Konečný V., Lexa J. & Žec B. 2002: Geochronology of the Neogene volcanism in the Vihorlatské vrchy mountain range, eastern Slovakia. *Geol. Carpath.* 53, special issue: Proceedings of XVII. Congress of Carpathian–Balkan Geological Association Bratislava, September 1–4. http://www.geologicacarpathica.com/special-issues/53-2002/#p

Pécskay Z., Lexa J., Szakács A., Seghedi I., Balogh K., Konečný V., Zelenka T., Kovacs M., Póka T., Fülöp A., Márton E., Panaiotu C. & Cvetković V. 2006: Geochronology of Neogene magmatism in the Carpathian arc and intra-Carpathian area. *Geol. Carpath.* 57, 6, 511–530.

Peccerillo A. & Taylor S.R. 1976: Geochemistry of Eocene Calc–Alkaline Volcanic Rocks from the Kastamonu Area, Northern Turkey. *Contrib. Mineral. Petrol*. 58, 63–81.

Polák M., Plašienka D., Kohút M., Putiš M., Bezák V., Maglay J., Olšavský M., Havrila M., Buček S., Elečko M., Fordinál K., Nagy A., Hraško Ľ., Németh Z., Malík P., Liščák P., Madarás J., Slavkay M., Kubeš P., Kucharič Ľ., Boorová D., Zlínska A., Siráňová Z. & Žecová K. 2012: Explanations for the geological map of the Malé Karpaty Mts. 1:50 000. *State geological institute of Dionýz Štúr*, 1–287 (in Slovak).

Rieder M., Cavazzini G., D´yakonov Y.S. Frank-Kamenetskii V.A., Gottardi G., Guggenheim S., Koval P.V., Müller G., Neiva, A.M.R., Radoslovich E.W., Robert J-L., Sassi F.P., Takeda H., Weiss Z. & Wones D.R. 1998: Nomenclature of the micas. *Can. Mineral.* 36, 41–48.

Rocholl A., Boehme M., Guenther D., Höfer H. & Ulbig A. 2008: Prevailing stratospheric easterly wind direction in the Paratethys during Lower Badenian: Ar–Ar and Nd-isotopic evidence from rhyolitic ash layers in the Upper Freshwater Molasse, S-Germany. *Geophys. Res. Abstracts* 10, 1–2.

Roetzel R., de Leeuw A., Mandic O., Márton E., Nehyba S., Kuiper K., Scholger R. & Wimmer-Frey I. 2014: Lower Miocene (upper Burdigalian, Karpatian) volcanic ash fall at the south-eastern margin of the Bohemian Massif in Austria — New evidence from Ar/Ar-dating, palaeomagnetic, geochemical and mineralogical investigations. *Austrian J. Earth Sci.* 107, 2, 2–22.

Rybár S., Kováč M., Šarinová K., Halásová E., Hudáčková N., Šujan M., Kováčová M. & Ruman A. 2016: Neogene changes in Paleogeography, Paleoenvironment and the Provenance of sediment in the Northern Danube Basin. *Bulletin of Geosciences* 91, 2, 367–398.

Sant K., Palcu D.V., Mandic O. & Krijgsman W. 2017: Changing seas in the Early–Middle Miocene of Central Europe: a Mediterranean approach to Paratethyan stratigraphy. *Terra Nov*a 29, 273–281.

Sant K., Kuiper K.F., Rybár S., Grunet P., Harzhauser M., Mandic O., Jamrich M., Krijgsman W., Šarinová K. & Hudáčková N.: Utilizing the highly sensitive mass spectrometer Argus VI+ for Ar/Ar tuff geochronology — examples from the key middle Miocene horizons of Central Paratethys. *Geol. Carpath.* (in press).

Seghedi I., Downes H., Szakács A., Mason P.R.D., Thirlwall M.F., Roşu E., Pécskay Z., Márton E. & Panaiotu C. 2004: Neogene–Quaternary magmatism and geodynamics in the Carpathian–Pannonian region: a synthesis. *Lithos* 72, 117–146

Sun S.-S. & McDonough W. F. 1989: Chemical and isotopic systematics of oceanic basalts: implications for mantle composition and processes. In: Sounders A.D. & Norry M.J. (Eds.): Magmatism in ocean basins. *Geological Society* 42, Special Issue, 313–345.

Szakács A., Pécskay Z., Silye L., Balogh K., Vlad D. & Fülöp A. 2012: On the age of the Dej Tuff, Transylvanian Basin (Romania). *Geol. Carpath.* 63, 2, 139–148.

Šimon L., Fordinál K., Kollarová V. & Kováčiková M. 2009: The Kuchyňa tuff — Finding of neovolcanics in Záhorie lowland. In: Kohút M. & Šimon L. (Eds): Spoločný Kongres Slovenskej a Českej Geologickej Spoločnosti. *Konferencie–Sympóziá–Semináre*, Bratislava, 1–262 (in Slovak).

Tagami T. & O'Sullivan P.B. 2005: Fundamentals of Fission-Track Thermochronology. *Rev. Mineral. Geochem.* 58, 1, 19–47.

Vass D., Nagy A., Kohút M. & Kraus I. 1988: Devínska Nová Ves Formation: Coarse clastic sedimets at the southeaster margin of the Viena Basin. *Mineralia Slovaca* 20, 2, 205–212.

Vass D. 2002: Lithostratigraphy of Western Carpathians, Neogene and Burda Paleogene. *State Geological Institute of Dionýz Štúr*, Bratislava, 1–200 (In Slovak).

White J.D.L. 1996: Impure coolants and interaction dynamics of phreatomagmatic eruptions. *J. Volcanol. Geotherm. Res.* 74, 155–170.

Supplement

The results from single grain $^{40}Ar/^{39}Ar$ dating of sanidine and biotite; x- grain selected for mean age calculation.

K4 — sample KU-s (sanidine) — 250–500 μm fraction Negative values in red

Age result PT4 (sanidine)	40(a)/36(a)	±2σ	40(r)/39(k)	±2σ	Age (Ma)	±2σ	MSWD	N	K/Ca ±2σ
Weighted mean age			1.82417	±0.00250	15.23	±0.04	2.58	22.71	25.0 ±20.4
				±0.14 %		±0.24 %	8 %	3	
					External error	±0.32	3.00	2σ Confidence Limit	
					Analytical Error	±0.02	1.6074	Error Magnification	
Normal Isochron	284.81	±9.94	1.82718	±0.00247	15.26	±0.04	0.58	22.71	
		±3.49 %		±0.14 %		±0.24 %	45 %	3	
					External error	±0.32	3.83	2σ Confidence Limit	
					Analytical Error	±0.02	1.0000	Error Magnification	
							1	Number of Iterations	
							0.0000000691	Convergence	
Inverse Isochron	287.02	±10.08	1.82650	±0.00253	15.25	±0.04	0.25	22.71	
		±3.51 %		±0.14 %		±0.24 %	62 %	3	
					External error	±0.32	3.83	2σ Confidence Limit	
					Analytical Error	±0.02	1.0000	Error Magnification	
							2	Number of Iterations	
							0.0001677194	Convergence	
							5 %	Spreading Factor	

K4 — sample KU-b (biotite) — 200–400 μm

Cannot be calculated — no reliable data

K4 — sample KU-s (sanidine) — 250–500μm fraction

Negative values in red

Relative abundances	Selected for mean age calc.	36Ar [fA]	%1σ	37Ar [fA]	%1σ	38Ar [fA]	%1σ	39Ar [fA]	%1σ	40Ar [fA]	%1σ	40(r)/39 (k) ± 2σ	Age ± 2σ	40Ar(r)	39Ar(k)	K/Ca ± 2σ
075_VU107-K4		0.0132193	4.140	7.174052	3.932	0.049756	21.501	4.0750	0.181	8.0108	0.156	1.13656 ± 0.08140	9.51 ± 0.68	57.75	0.25	0.2 ± 0.0
211_VU107-K4		0.0291440	2.582	1.212332	22.274	0.005477	215.355	0.8359	0.895	9.9421	0.091	1.59951 ± 0.54206	13.36 ± 4.51	13.43	0.05	0.3 ± 0.1
242_VU107-K4		0.0003642	113.798	7.243833	12.508	0.083863	11.446	4.0421	0.217	5.7919	0.174	1.60373 ± 0.07132	13.40 ± 0.59	111.79	0.25	0.2 ± 0.1
230_VU107-K4		0.0192783	3.589	1.458021	41.410	0.170930	4.131	12.3140	0.082	25.7768	0.043	1.63475 ± 0.03459	13.66 ± 0.29	78.09	0.75	3.6 ± 3.0
234_VU107-K4		0.0152665	3.295	6.170400	10.050	0.015649	68.741	1.9039	0.413	7.4708	0.127	1.78840 ± 0.16731	14.94 ± 1.39	45.48	0.12	0.1 ± 0.0
238_VU107-K4		0.0076510	6.213	2.201901	19.572	0.450208	1.782	34.9232	0.042	65.8318	0.022	1.81386 ± 0.00854	15.15 ± 0.07	96.23	2.13	6.8 ± 2.7
226_VU107-K4	x	0.0501951	0.807	0.378289	167.106	1.720144	0.590	139.8449	0.032	269.9246	0.009	1.82239 ± 0.00225	15.22 ± 0.02	94.42	8.51	159.0 ± 531.3
233_VU107-K4	x	0.0096753	5.678	0.129908	460.776	1.823573	0.586	148.3744	0.033	273.8608	0.006	1.82537 ± 0.00262	15.24 ± 0.02	98.90	9.03	491.1 ± 4526.0
239_VU107-K4	x	0.0034848	13.822	1.448549	40.360	1.052024	0.979	85.0259	0.034	156.5442	0.013	1.82672 ± 0.00379	15.25 ± 0.03	99.22	5.17	25.2 ± 20.4
072_VU107-K4		0.0167818	3.087	0.307118	70.271	2.776837	0.293	227.7500	0.031	421.7969	0.005	1.82928 ± 0.00180	15.28 ± 0.01	98.77	13.86	318.9 ± 448.2
266_VU107-K4		0.0247442	2.474	0.134052	201.821	2.678822	0.423	216.7077	0.032	404.2145	0.009	1.83029 ± 0.00209	15.28 ± 0.02	98.13	13.19	695.1 ± 2805.9
237_VU107-K4		0.0634326	0.968	1.076633	48.939	1.343396	0.748	106.7418	0.032	214.3803	0.008	1.83099 ± 0.00374	15.29 ± 0.03	91.17	6.50	42.6 ± 41.7
076_VU107-K4		0.0010689	51.639	0.328175	82.682	1.190355	0.841	96.5392	0.033	176.8512	0.017	1.83467 ± 0.00371	15.32 ± 0.03	100.15	5.87	126.5 ± 209.2
073_VU107-K4		0.0191579	2.438	0.439096	50.843	3.235765	0.268	264.2576	0.032	493.2103	0.007	1.84405 ± 0.00162	15.40 ± 0.01	98.80	16.08	258.8 ± 263.1
241_VU107-K4		0.0378894	1.516	2.190971	42.256	1.006295	0.855	79.1695	0.036	158.0834	0.014	1.85533 ± 0.00494	15.49 ± 0.04	92.91	4.82	15.5 ± 13.1
232_VU107-K4		0.0634702	0.966	0.999862	48.595	2.211824	0.522	177.9574	0.032	351.6283	0.008	1.86816 ± 0.00246	15.60 ± 0.02	94.55	10.83	76.5 ± 74.4
229_VU107-K4		0.0043769	12.090	1.122332	59.607	0.547795	1.405	42.8203	0.043	79.4559	0.019	1.88745 ± 0.00798	15.76 ± 0.07	101.72	2.61	16.4 ± 19.6

K4 — sample KU-b (biotite) — 200–400 μm

Relative abundances	36Ar [fA]	%1σ	37Ar [fA]	%1σ	38Ar [fA]	%1σ	39Ar [fA]	%1σ	40Ar [fA]	%1σ	40(r)/39 (k) ± 2σ	Age ± 2σ	40Ar(r)	39Ar(k)	K/Ca ± 2σ
070_VU107-K5	1.4371723	0.221	0.2366880	90.996	1.2446337	0.731	67.39425	0.039	516.90946	0.007	1.30299 ± 0.03113	10.89 ± 0.26	16.99	49.51	122 ± 223
064_VU107-K5	0.1323083	0.533	0.2211982	109.773	0.2120470	3.795	12.85359	0.074	60.47030	0.019	1.63224 ± 0.03363	13.64 ± 0.28	34.69	9.44	25 ± 55
066_VU107-K5	0.0975658	0.751	0.1241427	226.806	0.3252785	3.043	22.48018	0.055	67.73521	0.031	1.71629 ± 0.01993	14.34 ± 0.17	56.96	16.52	78 ± 353
067_VU107-K5	0.0706030	1.133	0.0569915	452.144	0.4854014	1.965	33.30935	0.043	81.11578	0.021	1.80201 ± 0.01457	15.05 ± 0.12	74.00	24.47	251 ± 2273
069_VU107-K5	0.0000030	15120.118	0.0218049	985.218	0.0057293	148.214	0.08031	12.135	0.30658	4.225	3.82740 ± 3.53960	31.82 ± 29.17	100.25	0.06	2 ± 31

K4 — sample KU-s (sanidine) — 250–500 μm fraction Negative values in red

Procedure Blanks	36Ar [fA]	1s	37Ar [fA]	1s	38Ar [fA]	1s	39Ar [fA]	1s	40Ar [fA]	1s
075_VU107-K4	0.0576419	0.0002875	0.0112875	0.0002127	0.0907446	0.0069851	0.0843214	0.0044608	12.8121465	0.0079092
211_VU107-K4	0.0462685	0.0005383	0.0114935	0.0002019	0.0982028	0.0073493	0.1112209	0.0033841	9.3666217	0.0062690
242_VU107-K4	0.0340295	0.0003026	0.0209043	0.0004184	0.0541622	0.0071173	0.0280898	0.0056539	6.6272261	0.0079850
230_VU107-K4	0.0370447	0.0004599	0.0207755	0.0002200	0.0313227	0.0035205	0.0329262	0.0058807	7.8470666	0.0081272
234_VU107-K4	0.0300846	0.0003327	0.0223419	0.0002316	0.0254738	0.0083092	0.0410613	0.0060767	5.5256340	0.0066072
238_VU107-K4	0.0300262	0.0003731	0.0222138	0.0001942	0.0331927	0.0057509	0.0297939	0.0033783	5.5774083	0.0048996
226_VU107-K4	0.0309244	0.0002346	0.0217698	0.0002382	0.0134130	0.0063271	0.0309833	0.0043349	5.7567186	0.0041848
233_VU107-K4	0.0300846	0.0003327	0.0223419	0.0002316	0.0254738	0.0083092	0.0410613	0.0060767	5.5256340	0.0066072
239_VU107-K4	0.0300262	0.0003731	0.0222138	0.0001942	0.0331927	0.0057509	0.0297939	0.0033783	5.5774083	0.0048996
072_VU107-K4	0.0472019	0.0003194	0.0114294	0.0001770	0.0807464	0.0050695	0.0762645	0.0036624	9.3936982	0.0078200
266_VU107-K4	0.0448238	0.0003445	0.0112556	0.0001523	0.0916567	0.0057580	0.0889090	0.0055367	8.9034586	0.0072972
237_VU107-K4	0.0300262	0.0003731	0.0222138	0.0001942	0.0331927	0.0057509	0.0297939	0.0033783	5.5774083	0.0048996
076_VU107-K4	0.0576419	0.0002875	0.0112875	0.0002127	0.0907446	0.0069851	0.0843214	0.0044608	12.8121465	0.0079092
073_VU107-K4	0.0472019	0.0003194	0.0114294	0.0001770	0.0807464	0.0050695	0.0762645	0.0036624	9.3936982	0.0078200
241_VU107-K4	0.0340295	0.0003026	0.0209043	0.0004184	0.0541622	0.0071173	0.0280898	0.0056539	6.6272261	0.0079850
232_VU107-K4	0.0300846	0.0003327	0.0223419	0.0002316	0.0254738	0.0083092	0.0410613	0.0060767	5.5256340	0.0066072
229_VU107-K4	0.0370447	0.0004599	0.0207755	0.0002200	0.0313227	0.0035205	0.0329262	0.0058807	7.8470666	0.0081272

K4 — sample KU-b (biotite) — 200–400 μm

Procedure Blanks	36Ar [fA]	1s	37Ar [fA]	1s	38Ar [fA]	1s	39Ar [fA]	1s	40Ar [fA]	1s
070_VU107-K5	0.0505644	0.0003093	0.0117142	0.0001730	0.0781906	0.0049747	0.0670506	0.0077162	10.436953	0.009939
064_VU107-K5	0.0451061	0.0003777	0.0114143	0.0001677	0.0909624	0.0044538	0.0798352	0.0052203	8.777078	0.005512
066_VU107-K5	0.0466496	0.0003859	0.0117590	0.0002199	0.0801151	0.0062311	0.0664830	0.0042479	9.244781	0.006819
067_VU107-K5	0.0466496	0.0003859	0.0117590	0.0002199	0.0801151	0.0062311	0.0664830	0.0042479	9.244781	0.006819
069_VU107-K5	0.0505644	0.0003093	0.0117142	0.0001730	0.0781906	0.0049747	0.0670506	0.0077162	10.436953	0.009939

Sample Parameters	Material	Standard (Ma)	%1s	J	%1s	MDF	%1s	Day	Time
075_VU107-K4	sanidine	28.201	0.08	0.004579	0.1	0.9944	0.03	8.2.17	18:27
211_VU107-K4	sanidine	28.201	0.08	0.004579	0.1	0.9944	0.03	14.3.17	19:54
242_VU107-K4	sanidine	28.201	0.08	0.004579	0.1	0.99286	0.03	14.3.17	13:18
230_VU107-K4	sanidine	28.201	0.08	0.004579	0.1	0.99286	0.03	14.3.17	8:53
234_VU107-K4	sanidine	28.201	0.08	0.004579	0.1	0.99286	0.03	14.3.17	10:08
238_VU107-K4	sanidine	28.201	0.08	0.004579	0.1	0.99286	0.03	14.3.17	11:14
226_VU107-K4	sanidine	28.201	0.08	0.004579	0.1	0.99286	0.03	13.3.17	16:58
233_VU107-K4	sanidine	28.201	0.08	0.004579	0.1	0.99286	0.03	14.3.17	9:49
239_VU107-K4	sanidine	28.201	0.08	0.004579	0.1	0.99286	0.03	14.3.17	11:32
072_VU107-K4	sanidine	28.201	0.08	0.004579	0.1	0.9944	0.03	8.2.17	17:34
266_VU107-K4	sanidine	28.201	0.08	0.004579	0.1	0.9944	0.03	16.2.17	12:03
237_VU107-K4	sanidine	28.201	0.08	0.004579	0.1	0.99286	0.03	14.3.17	10:53
076_VU107-K4	sanidine	28.201	0.08	0.004579	0.1	0.9944	0.03	8.2.17	18:45
073_VU107-K4	sanidine	28.201	0.08	0.004579	0.1	0.9944	0.03	8.2.17	17:52
241_VU107-K4	sanidine	28.201	0.08	0.004579	0.1	0.99286	0.03	14.3.17	12:59
232_VU107-K4	sanidine	28.201	0.08	0.004579	0.1	0.99286	0.03	14.3.17	9:30
229_VU107-K4	sanidine	28.201	0.08	0.004579	0.1	0.99286	0.03	14.3.17	8:34

Sample Parameters	Material	Standard (Ma)	%1s	J	%1s	MDF	%1s	Day	Time
070_VU107-K5	biotite	28.201	0.08	0.004579	0.1	0.9944	0.03	8.2.17	16:58
064_VU107-K5	biotite	28.201	0.08	0.004579	0.1	0.9944	0.03	8.2.17	15:12
066_VU107-K5	biotite	28.201	0.08	0.004579	0.1	0.9944	0.03	8.2.17	15:47
067_VU107-K5	biotite	28.201	0.08	0.004579	0.1	0.9944	0.03	8.2.17	16:05
069_VU107-K5	biotite	28.201	0.08	0.004579	0.1	0.9944	0.03	8.2.17	16:41

Information on Analysis and used Constants for samples of KU (K4: sanidine, K5: biotite)	
Analysis	
Material	sanidine, biotite
Location	Kuchyna, Slovakia
Analyst	K. Kuiper
Project	VU107
Mass Discr. Law	LIN
Irradiation	VU109
J (K4)	0.00457860±0.00000458
FCs	28.201±0.023 Ma
Heating	45 sec
Isolation	3.00 min
Instrument	ARGUS
Constants	
Age Equations	Min et al. (2000)
Negative Intensities	Allowed
Decay Constant 40K	5.460±0.053 E-10 1/a
Decay Constant 39Ar	2.940±0.016 E-07 1/h
Decay Constant 37Ar	8.230±0.012 E-04 1/h
Decay Constant 36Cl	2.257±0.015 E-06 1/a
Decay Activity 40K(EC,β^+)	3.310±0.030 1/gs
Decay Activity 40K(β^-)	27.890±0.150 1/gs
Atmospheric Ratio 40/36(a)	298.56±0.31
Atmospheric Ratio 38/36(a)	0.1885±0.0003
Production Ratio 39/37(ca)	0.000673±0.000004
Production Ratio 36/37(ca)	0.000264±0.000002
Production Ratio 40/39(k)	0.000860±0.000070
Production Ratio 38/39(k)	0.012110±0.000030
Production Ratio 36/38(cl)	262.80±1.71
Scaling Ratio K/Ca	0.43
Abundance Ratio 40K/K	1.1700±0.0100 E-04
Atomic Weight K	39.0983±0.0001 g